

# Coversheet

This document represents a preprint version of our research findings and is currently undergoing the initial stage of dissemination, having not yet undergone the rigorous process of peer review.

## **Title:**

Full Vector Inversion of Magnetic Microscopy Images Using Euler Deconvolution as A Priori Information

## **Authors:**

Gelson Ferreira Souza Junior - [gelson.ferreira@iag.usp.br](mailto:gelson.ferreira@iag.usp.br) - Universidade de São Paulo, Brazil

Leonardo Uieda - [Leonardo.Uieda@liverpool.ac.uk](mailto:Leonardo.Uieda@liverpool.ac.uk) - University of Liverpool, UK

Ricardo I. F. Trindade - [ricardo.trindade@iag.usp.br](mailto:ricardo.trindade@iag.usp.br) - Universidade de São Paulo, Brazil

Janine Carmo - [janine.carmo@iag.usp.br](mailto:janine.carmo@iag.usp.br) - Universidade de São Paulo, Brazil

Roger Fu - [rogerfu@fas.harvard.edu](mailto:rogerfu@fas.harvard.edu) - Harvard University, USA

Corresponding author: [Leonardo.Uieda@liverpool.ac.uk](mailto:Leonardo.Uieda@liverpool.ac.uk)

# Full vector inversion of magnetic microscopy images using Euler deconvolution as a priori information

Gelson Ferreira Souza Junior<sup>1\*</sup>, Leonardo Uieda<sup>2</sup>, Ricardo I. F. Trindade<sup>1</sup>, Janine Carmo<sup>1</sup>, and Roger Fu<sup>3</sup>

<sup>1</sup>Universidade de São Paulo, Brazil

<sup>2</sup>University of Liverpool, UK

<sup>3</sup>Harvard University, USA

\*Corresponding author: [gelson.ferreira@iag.usp.br](mailto:gelson.ferreira@iag.usp.br)

Received in original form on 2023/02/28.

**Disclaimer:** This is a non-peer reviewed preprint of an article submitted for publication in *Geochemistry, Geophysics, Geosystems*. It is available from EarthArXiv at <https://doi.org/XXXXX/XXXXXXX>.

**Open Science:** The source code used to generate all of the results presented in this research can be freely accessed and reused under the terms of an open license. You can find it at <https://doi.org/10.6084/m9.figshare.22672978> and <https://github.com/compgeolab/micromag-euler-dipole>.

**Keywords:** magnetic microscopy, geophysics, python, inverse problems, image processing

© 2023 The Authors. Available under the [Creative Commons Attribution 4.0 International License](https://creativecommons.org/licenses/by/4.0/) .

## Plain language summary

Very small magnetic particles in rocks and other materials can store information about what the Earth's magnetic field was like in the past. But not all particles are good recorders of this magnetic information, and some may have recorded different overlapping directions and strengths. So it is important to measure each particle separately in order to identify and separate the good recorders from the bad ones. A device called a “quantum diamond microscope” is able to measure the magnetic field near the surface of a rock sample at microscopic scale. We propose a new method for processing data from this microscope that is able to find out the individual magnetizations of large amounts of small magnetic particles automatically. We created a computer program to execute the method, which calculates the 3D position and magnetization of each particle using the simple model of a magnetic dipole. We tested the method on simulated data, using fake magnetic particles for which we know the correct magnetization and position, and real data, both of which showed good results in most cases. The method we created has the potential to enable the widespread study of the magnetism of natural materials with more detail than before.

## Abstract

Paleomagnetic data are usually obtained from whole cylindrical samples, where the signal results from the sum of magnetic moments from hundreds of thousands to millions of magnetic particles within the sample volume. This usually includes both stable and unstable remanence carriers. Recently, magnetic microscopy techniques allowed the investigation of individual grains by directly imaging their magnetic field. However, the determination of the magnetic moments of individual grains is hindered by the intrinsic ambiguity in the inversion of potential field data, as well as by the large number of grains found in any one microscopy image. We present a fast, semi-automated algorithm capable of estimating the position and magnetization of each ferromagnetic (l.s) source using only the magnetic microscopy data. Our algorithm works in three steps: (i) we first apply image

processing techniques to identify and isolate data window boundaries for each source; (ii) with these window boundaries, the position of the sources is estimated using Euler deconvolution; and finally (iii) using the position information, the algorithm is able to estimate the magnetic dipole moment direction and intensity for each source through an overdetermined linear inverse problem using a dipolar approximation. The method does not require any type of additional information about the sample or the sources. Sensitivity tests were run to estimate the stability of our routine to the depth of particles, signal-to-noise ratio, and non-dipolarity of the sources. Tests with simple synthetic data show the high effectiveness of the methodology for recovering the position and magnetic information for both dipolar and non-dipolar sources. More complex synthetic data including over 100 different magnetic particles were devised to emulate real rock data. Results obtained on these data also show the feasibility and robustness of the algorithm to semi-automatically estimate the position and magnetic moment of a large number of particles. This is further confirmed through an application to real data in which we are able to retrieve the expected bimodal isothermal remanent directions that were induced in the sample. Given its semi-automatic nature, its low processing cost, and the possibility of simultaneous inversion of the magnetic moment of a great number of magnetic particles, the methodology here proposed is a step forward in enabling paleomagnetic applications of magnetic microscopy.

## 1 Introduction

Several branches of Earth Sciences have demonstrated the importance of spatial resolution on a microscopic scale. For example, geochemistry and geochronology applications have benefited from point-wise analyses and compositional maps, allowing significant advances in the understanding of igneous, metamorphic and sedimentary processes (Barnes et al., 2019; Davidson et al., 2007; Verberne et al., 2020). Classical paleomagnetic techniques, on the other hand, consist of analyzing bulk samples, where the magnetic signal of a single specimen is the result of the sum of moments of a large assembly of ferromagnetic grains (Dunlop and Özdemir, 1997). Typically, a standard paleomagnetic sample of approximately  $10\text{ cm}^3$  would contain hundreds of thousands to millions of magnetic particles with sizes varying from magnetically stable single-domain (SD) and vortex state grains (also called pseudo-single domain, PSD) with sizes below  $1\text{ }\mu\text{m}$ , to large ( $\gg 1\text{ }\mu\text{m}$ ) grains with multi-domain (MD) magnetic structures, which are less stable magnetic recorders (Berndt et al., 2016). These large MD grains usually conceal the signal of the SD and PSD grains, and techniques of step-wise thermal and magnetic treatments are needed to unveil this more stable and reliable magnetic record (Tauxe et al., 2018). Recently, magnetic microscopy techniques opened the possibility of obtaining magnetic field maps at the micro-scale and recovering the magnetization of each grain, therefore enabling the separate analysis of stable and unstable magnetic particles (de Groot et al., 2014, 2018; Lima et al., 2014; Weiss et al., 2007).

In order to apply magnetic microscopy to paleomagnetic studies, it is necessary to recover from the magnetic images a large number of individual magnetic moments, corresponding to at least tens of thousands of stable fine-grained grains ( $< 1\text{ }\mu\text{m}$ ), in order to provide statistical significance to the remanence vector (e.g., Berndt et al., 2016). Nowadays, with the development of magnetic microscopy techniques, this task is no longer limited by the resolution of magnetic microscopes (de Groot et al., 2018; Fu et al., 2020; Glenn et al., 2017; Lima et al., 2014; Weiss et al., 2007), but essentially by the intrinsic problem presented by the ambiguity in the inversion of potential field data (Barbosa and Silva, 2011; de Groot et al., 2021; Oliveira Jr. et al., 2015), and ultimately by the lack of a fast and automated way to recover such a large number of individual magnetic moments from a set of magnetic images (Cortés-Ortuño et al., 2022; Lima and Weiss, 2009; Lima et al., 2013).

A solution to the non-uniqueness of magnetic moment inversion is to add independent prior information, such as the position of the ferromagnetic particles (Fabian and de Groot, 2019). This can be obtained, for example, from X-ray computed tomography (microCT; de Groot et al., 2021, 2018; Fabian and de Groot, 2019). Nonetheless, the standard microCT techniques do not provide adequate resolution to resolve the finer and more stable magnetic grains (Cortés-Ortuño et al., 2022; de Groot et al., 2021), whereas other more sophisticated techniques such as ptychographic X-ray tomography (e.g., Maldanis et al., 2020) are not readily available and too time-consuming to be routinely used in paleomagnetic studies.

Another route to be explored in the inversion of magnetic microscopy images is to obtain all the information, i.e. the magnetic moment and the position of the sources, from the magnetic data itself (e.g., Fu et al., 2020). For that, we can explore the techniques developed in exploration geophysics, in spite of the differences between aeromagnetic surveys and magnetic microscopy (Lima et al., 2013). Magnetic microscopy images commonly show the combined signal of multiple magnetic particles and can vary greatly in wavelength, strength, and spatial separation, depending on the natural remanent magnetization (NRM) and location of each particle. We usually assume that the signal measured by the magnetic microscope is the vertical component of the magnetic induction vector ( $b_z$ ), the measurements are performed on a regular grid with evenly spaced grid points and at a constant height, and the data are contaminated with pseudorandom Gaussian noise and long-wavelength noise (akin to a regional signal in aeromagnetic data). Here, we provide a methodological routine to retrieve the individual magnetic moment of ferromagnetic grains in magnetic microscopy images following the approach devised by Oliveira Jr. et al. (2015) for the interpretation of aeromagnetic anomalies. The method we propose allows one to quickly and semi-automatically estimate the individual magnetic moment vector of the stable magnetic carriers, making use of only the magnetic images themselves and an assumption of approximately dipolar sources. If used on a large scale, the method provides the means to scan large areas of the rock sample, attaining potentially the number of magnetic moments necessary for paleomagnetic studies.

## 2 Methodology

We will achieve the goal of estimating the dipole moment of several individual grains per image in a semi-automatic fashion by dividing the task into three parts that can be performed independently:

1. **Source detection and separation:** Identify and spatially isolate the magnetic field caused by each source. We will do this through a combination of classic potential field data processing (*total gradient amplitude*) and image processing (histogram stretching and equalization) and segmentation methods (watershed segmentation).
2. **Position estimation:** Estimate the 3D position of a magnetic particle based on the magnetic field measurements and the assumption of a dipolar source. This can be achieved by applying the Euler Deconvolution method to the data segment identified in step 1.
3. **Magnetic moment inversion:** Estimate the 3-component dipole moment vector by inverting the magnetic field data using the position obtained from Euler Deconvolution as a constraint and the assumption of a dipolar source. This leads to a linear inverse problem that is stable and computationally efficient, particularly since the inversion is performed separately for each data segment identified in step 1.

In the sections below, we describe the methodology used in each step of our proposed workflow.

## 2.1 Automatic source detection and separation

Our first task is to automatically identify the signal of individual particles and spatially segregate the data into windows, each containing the signal of a single particle. We implemented the following workflow to achieve this:

1. Calculate the *total gradient amplitude* (TGA), also known as the 3D analytic signal (Roest et al., 1992), of the observed vertical component of the magnetic field. The TGA is entirely positive and tends to be more concentrated on top of the magnetic field sources than the observed magnetic field. The derivative calculation also acts as a high-pass filter, removing long-wavelength noise from the data.
2. Apply a contrast stretching method to re-scale the TGA to a new range defined by the lower and upper percentiles of the data in order to highlight the weaker signals, either coming from small or from deep-seated particles.
3. Use the Laplacian of Gaussian (LoG) method (Van der Walt et al., 2014) on the re-scaled TGA data to estimate the position and size of data windows containing the signal of each particle.

The total gradient amplitude (TGA) was devised as a filter that can be applied to aeromagnetic data to reduce the signal's dependence on the direction of magnetization of the source and that concentrates the signal above the sources (Nabighian et al., 2005; Roest et al., 1992). The TGA is defined as the norm of the gradient vector of a scalar field  $f(x, y, z)$

$$\|\vec{\nabla}f(x, y, z)\| = \sqrt{(\partial_x f)^2 + (\partial_y f)^2 + (\partial_z f)^2}, \quad (1)$$

in which  $\partial_x f$  is the partial derivative of  $f$  with respect to  $x$  and likewise for the  $y$  and  $z$  directions. The partial derivatives are best approximated using a second-order accurate central finite-difference scheme

$$\partial_x f(x, y, z) \approx \frac{f(x + \Delta x, y, z) - f(x - \Delta x, y, z)}{2\Delta x}, \quad (2)$$

and likewise for the  $y$  and  $z$  directions, in which  $\Delta x$  is the grid spacing (assumed to be equal in the  $x$  and  $y$  directions). For the  $z$  component,  $\Delta z = \Delta x$  and  $f(x, y, z + \Delta z)$  and  $f(x, y, z - \Delta z)$  are calculated by upward and downward continuation, respectively, performed in the wavenumber domain. The 2D maps of the  $x$ ,  $y$ , and  $z$  derivatives will also be used in the Euler Deconvolution step described below, which is known to be highly sensitive to noise in the derivatives (Saleh and Pašteka, 2012). This is why we prefer the finite-differences based derivatives, which are less prone to amplifying short-wavelength noise than those calculated in the wavenumber domain through the Fast Fourier Transform (FFT).

Once we have obtained a TGA image, we apply a contrast stretching method to re-scale the TGA values in order to highlight the weaker signals present in the image. This is a necessary step to make sure that the blob detection algorithm is able to identify particles causing both weak and strong signals. The following contrast stretching operation is performed per pixel of the TGA image

$$\text{TGA}_{rescaled} = 2 \left( \frac{\text{TGA} - v_{min}}{v_{max} - v_{min}} \right) - 1, \quad (3)$$

in which  $v_{min}$  and  $v_{max}$  are the upper and lower bounds of TGA values that will be stretched to the range  $[0, 1]$ . By experimentation, we found that values of  $v_{min} = 1^{\text{st}}$  and  $v_{max} = 99^{\text{th}}$  percentiles of

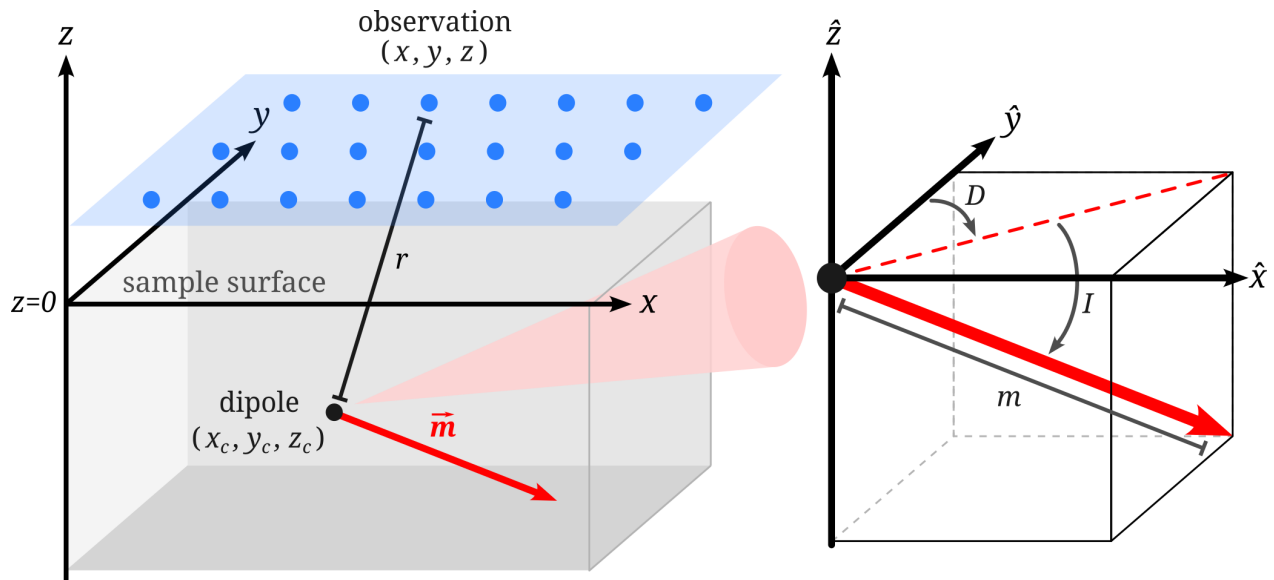


**Figure 1:** Schematic representation of the coordinate systems and modelling elements. The left panel shows the  $x, y, z$  right-handed coordinate system with  $z$  pointing upward and away from the sample. The top surface of the sample defines the  $z = 0$  surface. A dipole with dipole moment vector  $\mathbf{m}$  is also shown at coordinates  $(x_c, y_c, z_c)$ . The observation points are located at regular intervals on an  $x - y$  plane at a positive  $z$  separation from the sample surface. The right panel zooms in on the dipole and shows the dipole moment vector expressed in terms of inclination ( $I$ , positive downwards), declination ( $D$ , angle with the  $\hat{y}$  direction), and moment magnitude  $m = \|\mathbf{m}\|$ .

the TGA range work well on real magnetic microscopy datasets.

The re-scaled TGA image is then used as input for a Laplacian of Gaussian (LoG) blob detection algorithm (Kong et al., 2013). This method is able to identify the location and size of multiple windows in the image containing “blobs”. In our case, the blobs are the re-scaled TGA field of each particle and the LoG method detects the local TGA maxima. The LoG method is particularly well suited for the detection of bright blobs on a dark background at the expense of a longer computation time (Han and Uyyanonvara, 2016). For the image sizes routinely found in magnetic microscopy, the computation is fast and only needs to be performed once per image.

## 2.2 Euler Deconvolution

Once the locations and sizes of the windows containing the isolated signals of each particle are determined, we can apply the Euler Deconvolution (ED) estimate of the  $x, y,$  and  $z$  positions of the center of the particles under a dipolar approximation. This technique was first proposed by Thompson (1982) under the name EULDPH and later extended to three dimensions and renamed “Euler Deconvolution” by Reid et al. (1990). ED is traditionally performed on a set of moving windows that scan the entire dataset, producing a large scatter of position estimates, most of which are spurious (Silva and Barbosa, 2003). This is only done because it is impractical to segment an aeromagnetic dataset into individual anomalies. Fortunately, magnetic microscopy images often contain fewer elongated features (e.g., dikes and suture zones) and regional signals (e.g., Curie depth variations) that are difficult to separate. This makes it possible for us to produce isolated signals for each magnetic particle through the source detection step described above. Since each data window contains only the signal of a single particle, we are able to apply ED and generate only a single position estimate per particle.

Euler Deconvolution is formulated as a least-squares inversion of Euler’s homogeneity equation

$$(x - x_c)\partial_x f + (y - y_c)\partial_y f + (z - z_c)\partial_z f = (b - f)\eta, \quad (4)$$

in which  $(x_c, y_c, z_c)$  are the coordinates of the magnetic field source (Figure 1),  $b$  is the base level representing a constant shift in the signal, and  $\eta$  is the structural index corresponding to the nature of the source (Reid et al., 1990). This equation holds true for simple geometric sources, like spheres, dipoles, and vertical cylinders. Here, we assume that the magnetic particles are small enough and the sensor is far enough away that the sources can be represented by dipoles, yielding an  $\eta = 3$ .

The inversion is performed by rearranging Equation 4 into a pseudo-parametric model with parameters  $x_c, y_c, z_c$ , and  $b$

$$x_c\partial_x f + y_c\partial_y f + z_c\partial_z f + \eta b = x\partial_x f + y\partial_y f + z\partial_z f + \eta f. \quad (5)$$

Given a set of  $N$  observations of the magnetic field as the harmonic function  $f$  and its spatial derivatives, we can form the  $N \times 4$  system of equations

$$\begin{bmatrix} \partial_x f_1 & \partial_y f_1 & \partial_z f_1 & \eta \\ \partial_x f_2 & \partial_y f_2 & \partial_z f_2 & \eta \\ \vdots & \vdots & \vdots & \vdots \\ \partial_x f_N & \partial_y f_N & \partial_z f_N & \eta \end{bmatrix} \begin{bmatrix} x_c \\ y_c \\ z_c \\ b \end{bmatrix} = \begin{bmatrix} x_1\partial_x f_1 + y_1\partial_y f_1 + z_1\partial_z f_1 + \eta f_1 \\ x_2\partial_x f_2 + y_2\partial_y f_2 + z_2\partial_z f_2 + \eta f_2 \\ \vdots \\ x_N\partial_x f_N + y_N\partial_y f_N + z_N\partial_z f_N + \eta f_N \end{bmatrix}. \quad (6)$$

In matrix notation, this linear system can be written as

$$\mathbf{G}\mathbf{p} = \mathbf{h}. \quad (7)$$

We can arrive at a solution to Equation 7 by assuming that the three spatial derivatives of  $f$  have negligible error and minimizing the misfit  $\phi(\mathbf{p})$  between a pseudo-observation vector  $\mathbf{h}^o$  and the predictions  $\mathbf{h}$ . The least-squares misfit  $\phi(\mathbf{p})$  is defined as

$$\phi(\mathbf{p}) = \|\mathbf{h}^o - \mathbf{h}\|^2 = (\mathbf{h}^o - \mathbf{G}\mathbf{p})^T (\mathbf{h}^o - \mathbf{G}\mathbf{p}). \quad (8)$$

The minimum of  $\phi(\mathbf{p})$  is obtained by solving the  $4 \times 4$  system of normal equations

$$\mathbf{G}^T \mathbf{G}\mathbf{p} = \mathbf{G}^T \mathbf{h}^o. \quad (9)$$

The solution vector  $\hat{\mathbf{p}}$  provides an estimate of the position  $(x_c, y_c, z_c)$  and base level  $b$  for the source located inside of a data window. Repeating this process for each window produced by the source detection algorithm will yield the horizontal locations and depths of each magnetic particle.

### 2.3 Magnetic moment inversion

Once the source position is known and we can assume that it is approximately spherical or dipolar, we can apply the method developed by Oliveira Jr. et al. (2015) to estimate the dipole moment vector  $\mathbf{m}$  of the source. We begin by following Oliveira Jr. et al. (2015) in formulating the magnetic induction vector  $\mathbf{b}$  of a dipole as

$$\mathbf{b} = \begin{bmatrix} b_x \\ b_y \\ b_z \end{bmatrix} = \frac{\mu_0}{4\pi} \begin{bmatrix} \frac{\partial^2}{\partial x \partial x} \frac{1}{r} & \frac{\partial^2}{\partial x \partial y} \frac{1}{r} & \frac{\partial^2}{\partial x \partial z} \frac{1}{r} \\ \frac{\partial^2}{\partial y \partial x} \frac{1}{r} & \frac{\partial^2}{\partial y \partial y} \frac{1}{r} & \frac{\partial^2}{\partial y \partial z} \frac{1}{r} \\ \frac{\partial^2}{\partial z \partial x} \frac{1}{r} & \frac{\partial^2}{\partial z \partial y} \frac{1}{r} & \frac{\partial^2}{\partial z \partial z} \frac{1}{r} \end{bmatrix} \begin{bmatrix} m_x \\ m_y \\ m_z \end{bmatrix} = \frac{\mu_0}{4\pi} \mathbf{M} \mathbf{m}, \quad (10)$$

in which  $r = \sqrt{(x - x_c)^2 + (y - y_c)^2 + (z - z_c)^2}$  is the Cartesian distance between the observation point  $(x, y, z)$  and the source  $(x_c, y_c, z_c)$  and  $\mu_0$  is the vacuum magnetic permeability. Most magnetic microscopes provide measurements of only the vertical component  $b_z$ , which can be isolated from Equation 10 as shown in Equation 11, which is a similar approach to the uniform model proposed by Weiss et al. (2007).

$$b_z = \frac{\mu_0}{4\pi} \begin{bmatrix} \frac{\partial^2}{\partial z \partial x} \frac{1}{r} & \frac{\partial^2}{\partial z \partial y} \frac{1}{r} & \frac{\partial^2}{\partial z \partial z} \frac{1}{r} \end{bmatrix} \begin{bmatrix} m_x \\ m_y \\ m_z \end{bmatrix} = \frac{\mu_0}{4\pi} \mathbf{M}_z \mathbf{m}. \quad (11)$$

The three second-order derivatives in Equation 11 are

$$\begin{aligned} \frac{\partial^2}{\partial z \partial x} \frac{1}{r} &= \frac{3(z - z_c)(x - x_c)}{r^5}, \\ \frac{\partial^2}{\partial z \partial y} \frac{1}{r} &= \frac{3(z - z_c)(y - y_c)}{r^5}, \\ \frac{\partial^2}{\partial z \partial z} \frac{1}{r} &= \frac{3(z - z_c)^2}{r^5} - \frac{1}{r^3}. \end{aligned} \quad (12)$$

Given a set of  $N$  observations of  $b_z$  made inside a window containing a single source, we can form the  $N \times 3$  linear equation system

$$\begin{bmatrix} \frac{\mu_0}{4\pi} \frac{3(z_1 - z_c)(x_1 - x_c)}{r_1^5} & \frac{\mu_0}{4\pi} \frac{3(z_1 - z_c)(y_1 - y_c)}{r_1^5} & \frac{\mu_0}{4\pi} \left( \frac{3(z_1 - z_c)^2}{r_1^5} - \frac{1}{r_1^3} \right) \\ \frac{\mu_0}{4\pi} \frac{3(z_2 - z_c)(x_2 - x_c)}{r_2^5} & \frac{\mu_0}{4\pi} \frac{3(z_2 - z_c)(y_2 - y_c)}{r_2^5} & \frac{\mu_0}{4\pi} \left( \frac{3(z_2 - z_c)^2}{r_2^5} - \frac{1}{r_2^3} \right) \\ \vdots & \vdots & \vdots \\ \frac{\mu_0}{4\pi} \frac{3(z_N - z_c)(x_N - x_c)}{r_N^5} & \frac{\mu_0}{4\pi} \frac{3(z_N - z_c)(y_N - y_c)}{r_N^5} & \frac{\mu_0}{4\pi} \left( \frac{3(z_N - z_c)^2}{r_N^5} - \frac{1}{r_N^3} \right) \end{bmatrix} \begin{bmatrix} m_x \\ m_y \\ m_z \end{bmatrix} = \begin{bmatrix} b_{z1} \\ b_{z2} \\ \vdots \\ b_{zN} \end{bmatrix}, \quad (13)$$

which can also be expressed in matrix form as

$$\mathbf{A} \mathbf{m} = \mathbf{d}. \quad (14)$$

As with Euler Deconvolution, we can find a dipole moment vector that best fits a set of  $N$  observations of the vertical component of the magnetic field  $\mathbf{d}^o$  in a least-squares sense by minimizing the misfit function

$$\Gamma(\mathbf{m}) = \|\mathbf{d}^o - \mathbf{d}\|^2 = (\mathbf{d}^o - \mathbf{A}\mathbf{m})^T (\mathbf{d}^o - \mathbf{A}\mathbf{m}). \quad (15)$$

The dipole moment vector that minimizes  $\Gamma(\mathbf{m})$  can be found by solving the  $3 \times 3$  normal equation system

$$\mathbf{A}^T \mathbf{A} \mathbf{m} = \mathbf{A}^T \mathbf{d}^o. \quad (16)$$

The estimated dipole moment vector  $\hat{\mathbf{m}}$  can be converted into declination  $D$ , inclination  $I$ , and magnitude  $m$ , which are more intuitive quantities for interpreting paleomagnetic results, like so (Tauxe et al., 2018)

$$\begin{aligned} I &= \tan^{-1} \frac{m_z}{\sqrt{m_x^2 + m_y^2}}, \\ D &= \tan^{-1} \frac{m_x}{m_y}, \\ m &= \sqrt{m_x^2 + m_y^2 + m_z^2}. \end{aligned} \quad (17)$$

It is important to note that these are not paleomagnetic declination and inclination angles, but are instead related to the sample coordinate system. To obtain the paleomagnetic direction, the dipole moment vector must be rotated to the sample field orientation prior to the application of Equation 17.

In a micromagnetic survey, or any geophysical survey, measurements are affected by noise caused by experimental errors, equipment inaccuracies, and sensor limitations. This noise will affect the estimated parameter vector  $\hat{\mathbf{m}}$ , regardless of the method used. Assuming that the noise in the observed data is independent and normally distributed with zero mean and variance  $\sigma_0^2$ , we can estimate the variance of the parameters by propagation of uncertainties. In reality, the data variance  $\sigma_0^2$  is rarely known and must be estimated using the  $\chi^2$  statistic (Aster et al., 2019)

$$\hat{\sigma}_0^2 = \chi^2 = \frac{\|\mathbf{d}^o - \mathbf{A}\hat{\mathbf{m}}\|^2}{N - 3}, \quad (18)$$

in which  $N - 3$  are the degrees-of-freedom. The covariance matrix  $\mathbf{C}$  of the estimated parameters is then given by (Aster et al., 2019)

$$\mathbf{C} = \hat{\sigma}_0^2 (\mathbf{A}^T \mathbf{A})^{-1} = \begin{bmatrix} \sigma_x^2 & \sigma_{xy} & \sigma_{xz} \\ \sigma_{yx} & \sigma_y^2 & \sigma_{yz} \\ \sigma_{zx} & \sigma_{zy} & \sigma_z^2 \end{bmatrix}. \quad (19)$$

From the main diagonal of  $\mathbf{C}$ , we can obtain the variances of the estimated declination  $\sigma_D^2$ , inclination  $\sigma_I^2$ , and magnitude  $\sigma_m^2$  by propagation of uncertainties from Equation 17

$$\begin{aligned}
\sigma_D^2 &= \frac{m_y^2 \sigma_x^2 + m_x^2 \sigma_y^2}{(m_x^2 + m_y^2)^2}, \\
\sigma_I^2 &= \frac{m_x^2 m_z^2 \sigma_x^2 + m_y^2 m_z^2 \sigma_y^2 + (m_x^2 + m_y^2)^2 \sigma_z^2}{(m_x^2 + m_y^2) m^4}, \\
\sigma_m^2 &= \frac{m_x^2 \sigma_x^2 + m_y^2 \sigma_y^2 + m_z^2 \sigma_z^2}{m^2}.
\end{aligned} \tag{20}$$

These variances reflect the sensitivity of the estimated dipole moment to random noise in the magnetic field observations. However, they do not capture other, often larger, sources of uncertainty like systematic errors in the observations, data positioning errors, and the validity of the dipolar approximation. Therefore, we recommend that these estimated variances be treated with caution and should not be interpreted as “the degree of certainty that the estimated values are the true values”.

Parameters retrieved during inversion procedures may not always explain the observed data perfectly. Hence, it is necessary to evaluate how well the predicted data is able to fit the observed data. When evaluating the goodness of fit of inversions of magnetic microscopy data, [Fu et al. \(2020\)](#) apply a “dipolarity parameter” ( $D$ ). We note that  $D$  is equivalent to the coefficient of determination

$$R^2 = 1 - \frac{\|\mathbf{d}^o - \mathbf{A}\hat{\mathbf{m}}\|^2}{\|\mathbf{d}^o - \bar{b}_z^o\|^2}, \tag{21}$$

in which  $\bar{b}_z^o$  is the mean of the observed data.  $R^2$  has a maximum value of 1, which indicates a perfect fit of the data. Values close to 1 can therefore be interpreted to mean that a simple dipole model is able to explain the observed data. On the other hand, low values of  $R^2$  indicate that the dipole model is not able to explain the observed data.

[Cortés-Ortuño et al. \(2021\)](#) use the “signal-to-noise ratio” (SNR) to evaluate the goodness of fit. Here, we define the SNR in a logarithmic decibel scale to make it independent of the scale of the data

$$\text{SNR} = 10 \log_{10} \frac{\sigma_d^2}{\sigma_r^2}, \tag{22}$$

in which  $\sigma_d^2$  is the variance of the observed data and  $\sigma_r^2$  is the variance of the residuals  $\mathbf{r} = \mathbf{d}^o - \mathbf{A}\hat{\mathbf{m}}$ . The SNR is the trade-off between the signal and its associated noise, which we approximate by the inversion residuals. The higher the SNR values (in decibels), the better the fit to the observed data. For a signal to be “visible”, [Strum and Fenigstein \(2014\)](#) suggest that  $\text{SNR} \geq 3$ , which means the signal is at least three times stronger than the noise. Here, we use both  $R^2$  and SNR as criteria for filtering out unreliable estimates from our dipole moment inversions.

### 3 Application to synthetic data

We first applied our inversion workflow to three sets of synthetic data to evaluate its strengths and limitations. The datasets are produced by different models of varying complexity which were designed to assess different aspects of the method.

1. **Method validation:** The first model is composed of a set of four dipoles with similar dipole moments amplitudes, but different inclinations and declinations. The synthetic data consists of

the vertical magnetic field ( $b_z$ ) derived from this model and contaminated by pseudo-random high-frequency noise. The purpose of this simple model is to investigate the efficiency of the combination of the source detection method, Euler deconvolution, and the dipole moment inversion under ideal circumstances, thus serving as a validation of the methodology.

2. **Applicability to non-dipolar sources:** The second model simulates a hundred sources with both dipolar and non-dipolar magnetic moments. Their vertical magnetic field ( $b_z$ ) is calculated at different sensor-source distances and is also contaminated with pseudo-random high-frequency noise. This model is used to assess the ability of the algorithm to deal with strong non-dipolar sources.
3. **Applicability to real-world scenarios:** The third model contains 103 dipoles with different dipole moment magnitudes, having inclinations and declinations clustered around two stable directions. The magnetic field generated from these sources is corrupted by both low and high-frequency noise. The complexity of this synthetic data seeks to more faithfully emulate real magnetic microscopy data.

### 3.1 Method validation

Figure 2a shows the vertical component of the magnetic field  $b_z$  over a synthetic rock section containing four dipolar sources. The map covers a surface of  $1000 \mu\text{m} \times 1000 \mu\text{m}$ , with data points in a regular grid with approximately  $1 \mu\text{m}$  spacing ( $N = 10^6$  observations) obtained at a sensor-sample distance of  $5 \mu\text{m}$ . The magnetic field data are contaminated with pseudo-random Gaussian noise with zero mean and 20 nT standard deviation.

We first applied an upward continuation filter (Figure 2b) to smooth out the high-frequency noise (Blakely, 1996). This is important because noise strongly affects the first derivatives of the field, which are required for the source detection algorithm and the Euler deconvolution. Then, we calculated the total gradient amplitude (Figure 2c), which was subjected to contrast stretching to highlight the weaker intensity sources as much as possible (Figure 2d). Subsequently, we applied the blob detection algorithm to the contrast-stretched total gradient amplitude to obtain the position of the data windows for each source (Figure 2e). Euler deconvolution was then performed for each data window identified by assuming a structural index  $\eta = 3$  of a point source, therefore obtaining the Cartesian coordinates (Figure 2f) of each source. For comparison, Table 1 shows the true and estimated values of the source coordinates.

The positions of each source obtained with Euler deconvolution were then used as input for the dipole moment inversion. The estimated dipole moment vectors are shown in Figure 3. Figure 3a shows the estimated dipole moment, along with the corresponding true values, as a stereonet for better comparison of the true and estimated vector directions. Figure 3b shows the estimate dipole moments overlaid on a map of the synthetic  $b_z$  to demonstrate the ability of our method to estimate a spatial distribution of dipole moments. For comparison, Table 1 also shows the true and estimate dipole moments as well as their corresponding standard deviations obtained using Equations 18-20.

### 3.2 Applicability to non-dipolar sources

Typically, when conducting magnetic field measurements with a large distance between the sensor and the magnetic anomaly source, higher-order non-dipole magnetization components such as quadrupoles and octupoles can be disregarded because of the strong attenuation with distance of

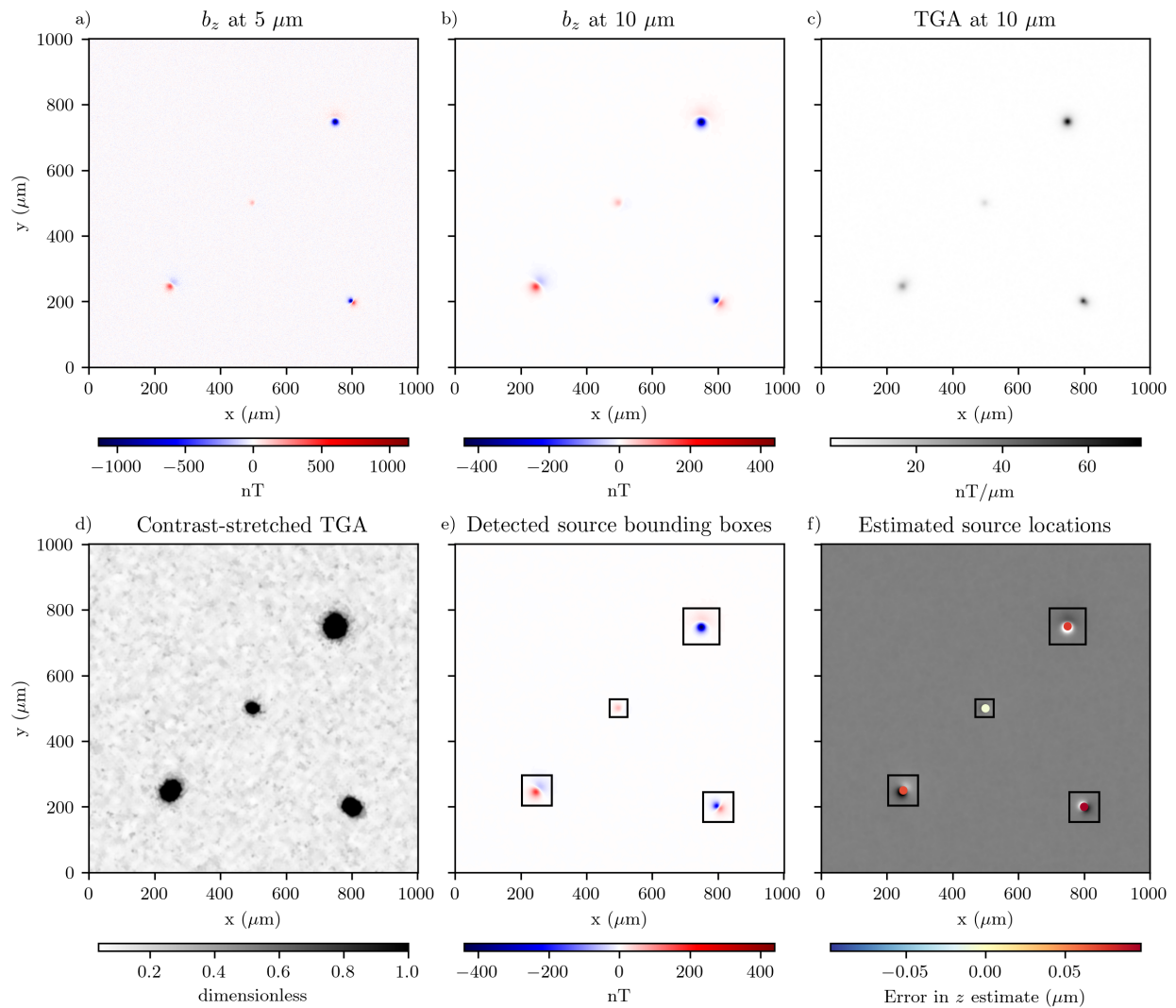


**Figure 2:** Simple synthetic data and the various processing steps performed prior to the dipole moment inversion. a) The synthetic noise-corrupted  $b_z$  observations at  $z = 5 \mu\text{m}$  due to four dipolar sources with different depths and dipole moment vectors (see Table 1). b) The upward-continued data to  $z = 10 \mu\text{m}$  showing attenuated short-wavelength noise. c) The total gradient amplitude (TGA) calculated from the upward-continued data, which is able to concentrate the signal on top of each dipolar source. d) The contrast-stretched TGA, highlighting the signal of all four sources, including the weak central source. e) The detected source bounding boxes (black squares) that correctly identify the signal of all four sources. f) The estimated source locations (colored circles) from Euler deconvolution of the upward-continued data inside each bounding box. The color represents the difference between the true and the estimated  $z$  coordinates.

the magnetic fields. However, in magnetic microscopy, where the sensor is positioned only a few microns from the sample, these higher-order components might be detected. This phenomenon is observed in paleomagnetic studies on particles with a PSD domain state, where magnetization is non-uniform throughout the grain. To assess the attenuation of these non-dipolar components and the applicability of our method, we conducted a simulation on particles with more complex magnetization at varying sensor-sample distances.

To simulate particles with non-dipolar magnetization components, we specified a spherical volume with a radius of approximately  $1 \mu\text{m}$ . Within this volume, we added 200 dipolar particles with varying dipole moment directions and amplitudes. These directions were generated randomly, fol-

	Position				Dipole moment		
	$x_c$ ( $\mu\text{m}$ )	$y_c$ ( $\mu\text{m}$ )	$z_c$ ( $\mu\text{m}$ )	$I$ ( $^\circ$ )	$D$ ( $^\circ$ )	$m$ ( $\text{A}\cdot\text{m}^2$ )	
true	800.00	200.00	-3.50	22.00	125.00	5.000e-15	
estimated	799.91	199.94	-3.40	$22.08 \pm 0.01$	$125.52 \pm 0.02$	$4.921\text{e-}15 \pm 1.4\text{e-}18$	
true	750.00	750.00	-8.50	62.00	10.00	1.500e-14	
estimated	749.98	749.99	-8.43	$62.00 \pm 0.01$	$9.30 \pm 0.02$	$1.486\text{e-}14 \pm 1.8\text{e-}18$	
true	250.00	250.00	-10.00	-30.00	-140.00	1.000e-14	
estimated	250.03	249.89	-9.93	$-30.32 \pm 0.01$	$-139.70 \pm 0.02$	$9.966\text{e-}15 \pm 2.6\text{e-}18$	
true	500.00	500.00	-7.75	-50.00	-70.00	2.000e-15	
estimated	500.07	499.95	-7.76	$-48.66 \pm 0.05$	$-70.36 \pm 0.09$	$2.000\text{e-}15 \pm 1.8\text{e-}18$	

**Table 1:** True and estimated source positions and dipole moments for the method validation test through a simple synthetic data application.

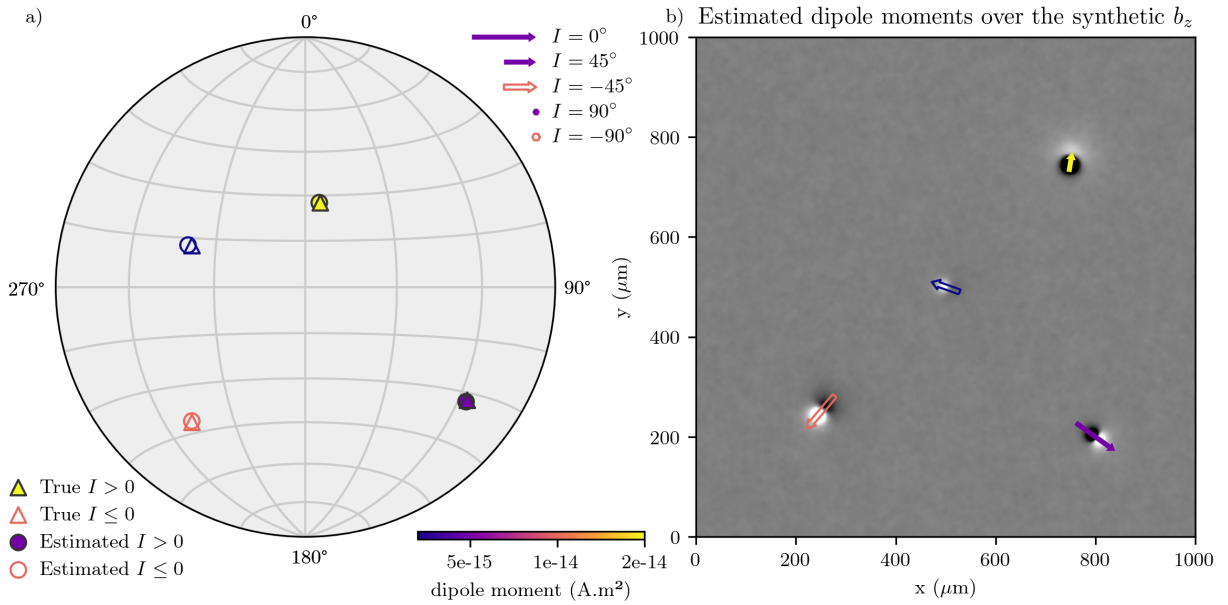


**Figure 3:** Comparison of true and estimated dipole moments for the method validation test through a simple synthetic data application. a) Stereonet showing the true (triangles) and estimated (circles) dipole moments. The colors are mapped to the dipole moment amplitude. b) Grayscale map of the synthetic  $b_z$  overlaid by the estimated dipole moment vectors. The vector locations were derived from the Euler deconvolution results, their size is inversely proportional to the inclination  $I$ , their direction represents the declination  $D$ , and their colors are mapped to the dipole moment amplitude using the same colorscale as the stereonet. In both graphs, solid symbols represent positive inclination while hollow symbols represent negative inclination.

lowing a normal distribution centered on the direction  $D = 90^\circ$  and  $I = 0^\circ$  and with a standard deviation of  $10^\circ$ . The dipole moment amplitudes were sampled by a normal distribution with mean  $10^{-14} \text{ A}\cdot\text{m}^2$  and standard deviation  $5 \times 10^{-14} \text{ A}\cdot\text{m}^2$ . We also randomly generated spatial positions around a central position of  $x_c = 25 \mu\text{m}$ ,  $y_c = 25 \mu\text{m}$ , and  $z_c = -1 \mu\text{m}$  with standard deviation of  $0.65 \mu\text{m}$ . The bulk magnetization of the non-dipolar particle is the vector sum of the dipole moments of each dipole. The centroid of the particle is defined by the average of the  $x_c$ ,  $y_c$ , and  $z_c$  positions of each dipole. The synthetic vertical magnetic field  $b_z$  of the non-dipolar source was calculated on regular grids with  $0.5 \mu\text{m}$  spacing. Each grid was located at a different sensor-sample distance

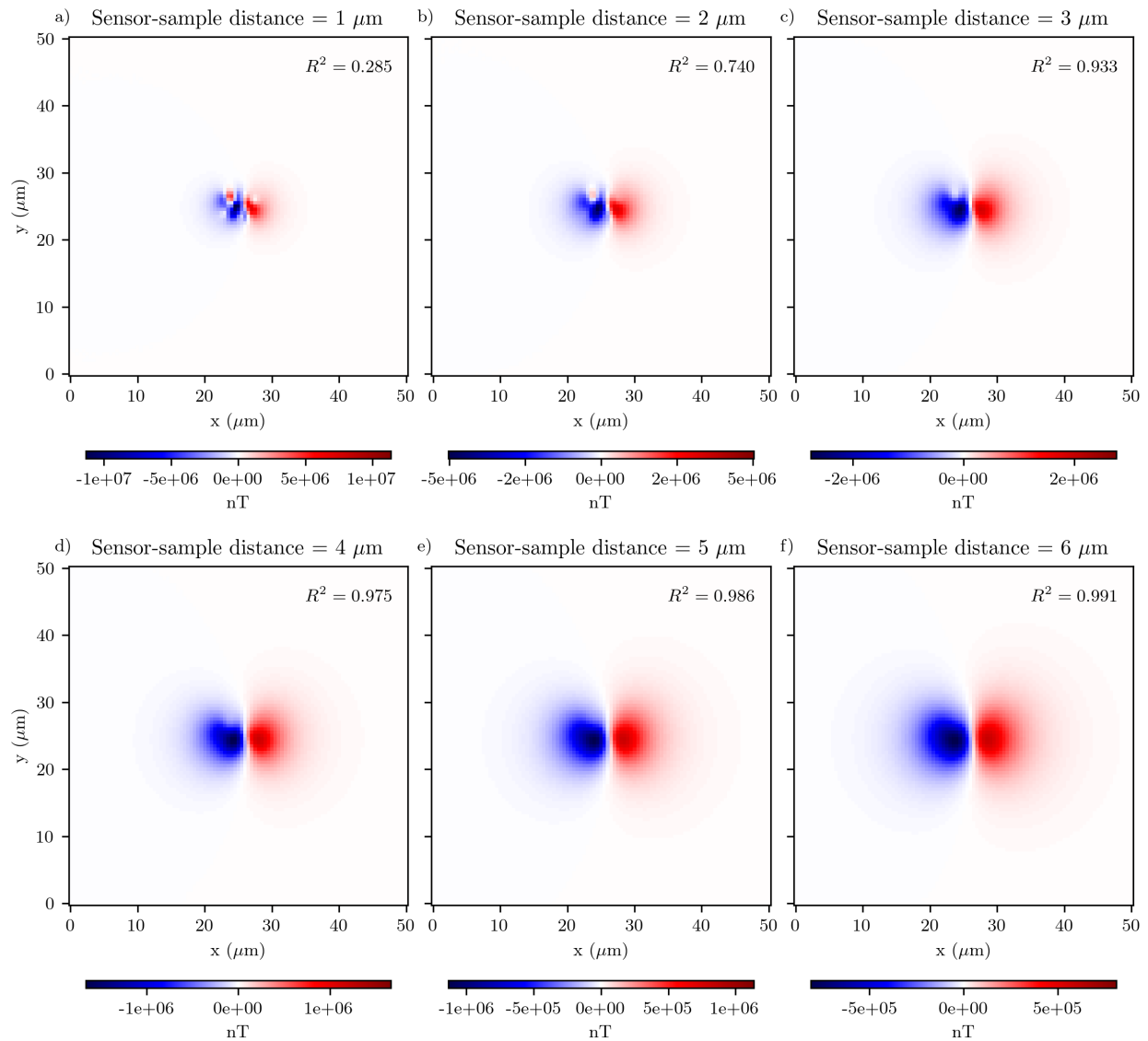


**Figure 4:** Caption: Simulated magnetic microscopy data for a spherical source with both dipolar and non-dipolar magnetic components. The distance from the sensor varies from 1  $\mu\text{m}$  to 6  $\mu\text{m}$  (a-f).

$z$ , varying between 1  $\mu\text{m}$  and 10  $\mu\text{m}$  in 0.5  $\mu\text{m}$  increments. The synthetic data were corrupted by pseudo-random Gaussian noise of mean 0 nT and a standard deviation of 20 nT. For each data grid generated, we performed Euler deconvolution to estimate the source position and subsequently inverted the data for the dipole moment. At each step, we recorded the inversion  $R^2$  value and the differences between the estimated position and dipole moment and the true centroid and bulk magnetization of the particle.

Figure 4 shows the synthetic  $b_z$  of an example non-dipolar particle at variable source-sample distances. When the particle is close to the sensor (1  $\mu\text{m}$  to 3  $\mu\text{m}$ ), the observed field is strongly non-dipolar (Figure 4a-b) and the dipole moment inversion produces low  $R^2$  values. As the distance increases, the magnetic field is attenuated, particularly the non-dipolar components which decay more rapidly than the dipolar component. This results in an increase in  $R^2$  (Figure 4c-d). At distances above 5  $\mu\text{m}$ , there is practically only the contribution of the dipolar component, causing  $R^2$  to approach its maximum value of 1 (Figure 4e-f).

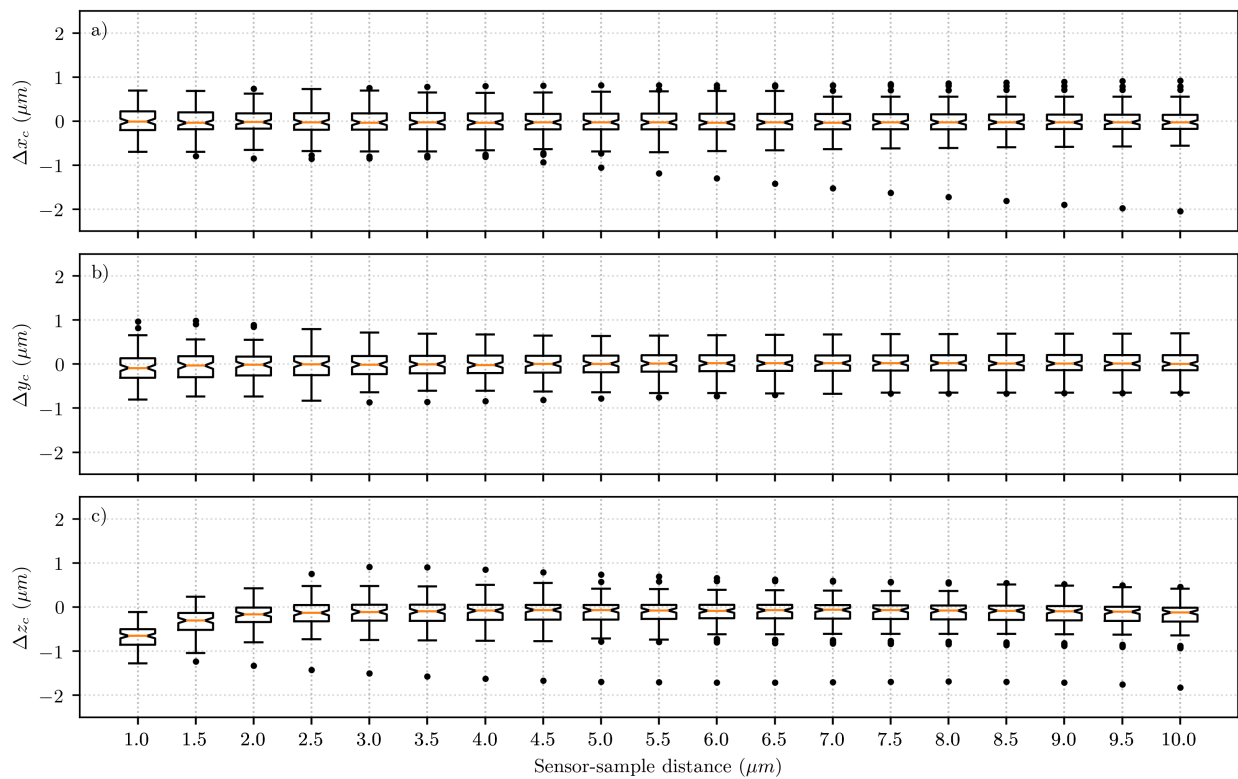


**Figure 5:** The simulation was randomly replicated ( $N=100$ ) to test the effectiveness of the Euler deconvolution in estimating the position of the modeled particles. The difference between the true position (centroid) and the estimated position was calculated for each replicate and plotted as a boxplot. The boxplot shows the distribution of differences in the (a)  $x_c$ , (b)  $y_c$ , and (c)  $z_c$ .

We replicated the particle generation procedure 100 times with variations in the randomness of magnetization and point particle positions. Subsequently, the Cartesian position of the spherical particle was estimated using ED, and the magnetization parameters were determined by inverting the magnetic field data. The effectiveness of position recovery was measured by comparing the particle's centroid with the solution of the Euler equation for  $x_c$ ,  $y_c$ , and  $z_c$  (Figure 5a, b, and c, respectively). As shown in Figure 5, ED estimates the positions of particles with more complex magnetization well, especially for sensor-source distances greater than  $5 \mu\text{m}$ , where the median of the distributions is centered at zero. However, when the sensor-source distance is small enough to emphasize the contribution from higher-order components, a lower degree of dipolarity is observed as expressed by lower values of  $R^2$  (Figure 6a). Consequently, in these cases, there are higher errors in the estimation of the direction of magnetization (Figure 6b) and in the magnetic moment's intensity (Figure 6c), which were expected since the inversion considers only the dipolar component. However, dipolarity significantly increases as the sensor to sample distance increases, while errors in direction and magnetic moment decrease significantly (Figure 6).

### 3.3 Applicability to real-world scenarios

This test represents a more complex scenario by simulating 103 sources randomly distributed in the imaged area of a synthetic thin section of  $2000 \mu\text{m} \times 2000 \mu\text{m}$ . The synthetic  $b_z$  data were generated on a regular grid with  $2 \mu\text{m}$  spacing and  $5 \mu\text{m}$  sensor-sample distance. We contaminated the data with high-frequency normally-distributed pseudo-random noise with zero mean and  $50 \text{ nT}$  standard

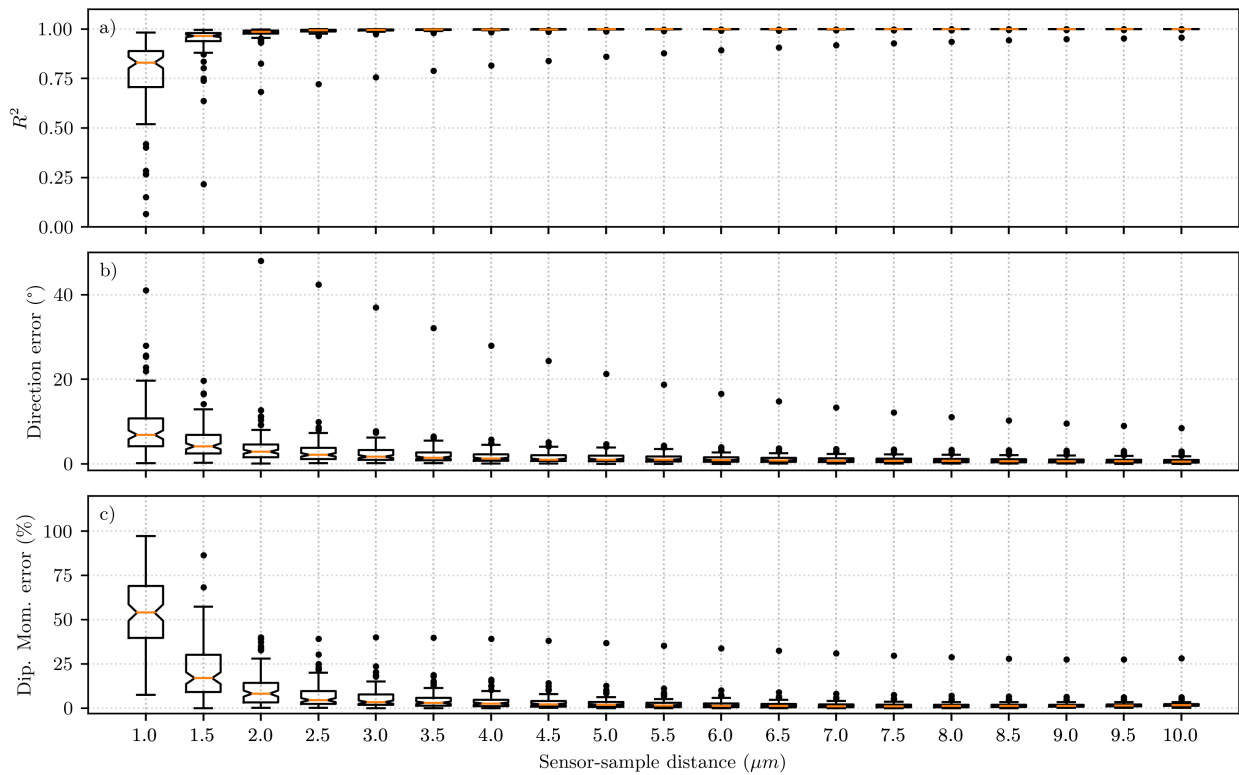


**Figure 6:** The simulation was randomly replicated ( $N=100$ ) to assess the accuracy of the algorithm in recovering the magnetic direction and moment of the modeled particles. The goodness of fit was measured by the R-squared value (a), while the angular error (b) and intensity error (c) between the real and modeled magnetic vector were plotted in degrees and percentages ( $|100 (m_{true} - m_{estimated}) / m_{true}|$ ), respectively.

deviation, as well as with low-frequency noise in the form of additional deep sources beyond the modeling domain.

For greater fidelity to real samples, the magnetic sources are modeled as dipoles with different depths and magnetic moment intensities. The depths vary randomly between 1 and 20  $\mu\text{m}$ , while the dipole moment intensities range randomly from  $10^{-12}$  to  $10^{-14}$   $\text{A m}^2$ . The NRM found in real ferromagnetic particles varies individually but averages out to the inducing field direction. To simulate this behavior in our synthetic data, we sample the source dipole moment directions from two pseudo-random Gaussian distributions. The first group of sources ( $M = 70$ ) are sampled from a distribution with mean of  $D = 0^\circ$  and  $I = 0^\circ$  and standard deviation of  $10^\circ$ . The second group of sources ( $M = 30$ ) are sampled from a distribution with mean of  $D = 180^\circ$  and  $I = 0^\circ$ , also with standard deviation of  $10^\circ$ . We also manually added 3 sources with higher dipole moments ( $5 \times 10^{-11}$ ) to further simulate the complexity observed in real data measurements. The noise-corrupted synthetic  $b_z$  data are shown in Figure 7a.

We then followed the same processing steps as for the simple synthetic: upward continuation (Figure 7b), TGA calculation (Figure 7c), contrast stretching (Figure 7d), blob detection (Figure 7e), and Euler Deconvolution (Figure 7e). A total of 99 sources out of the original 103 were successfully detected by our workflow.

The spatial resolution of the inversion results is one of the key advantages of magnetic microscopy over the classic techniques of paleomagnetism. Therefore, we present the inversion results spatially so that we can evaluate any patterns in their distribution. Figure 8 shows the spatial locations of

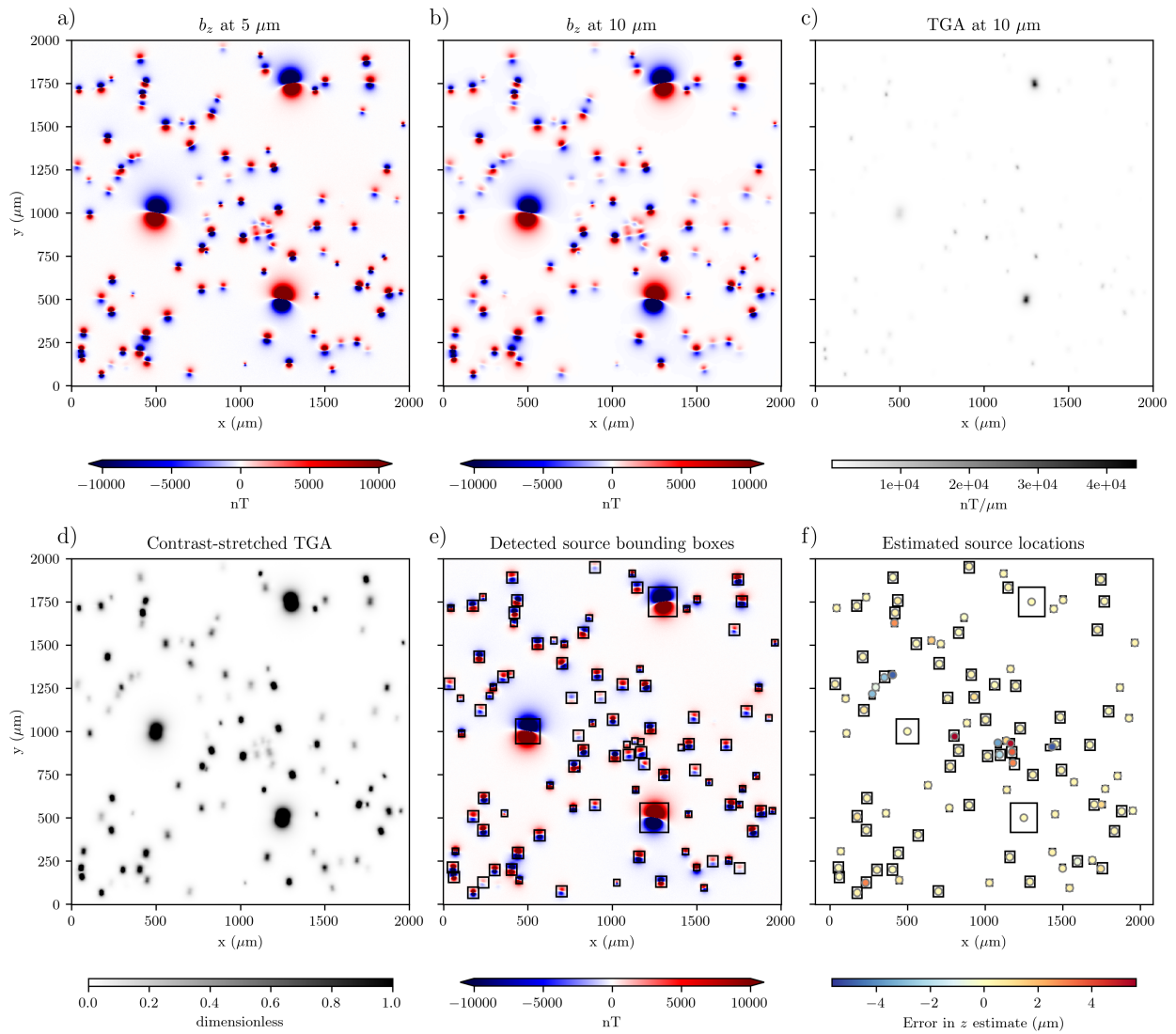


**Figure 7:** Complex synthetic data and the various processing steps performed prior to the dipole moment inversion. a) The synthetic high and low-frequency noise-corrupted  $b_z$  observations at  $z = 5 \mu\text{m}$  due to two clusters of stable directions simulated. b) Anomaly map after the upward-continued data to  $z = 10 \mu\text{m}$  to attenuated long and short-wavelength noise. c) The total gradient amplitude (TGA) calculated from the upward-continued data, which is able to concentrate the signal on top of each dipolar source. d) The contrast-stretched TGA, highlighting the signal of all sources, especially the weaker ones. e) The detected source bounding boxes (black squares) that correctly encapsulate the signal of the sources. f) The estimated source locations (colored circles) from Euler Deconvolution of the upward-continued data inside each bounding box. The color represents the difference between the true and estimated  $z$  coordinates.

the 99 sources that were identified and the differences between the estimated dipole moments and the true values. The depth and dipole moment amplitude of each source are represented by horizontal and vertical bars, respectively. These two variables are useful proxies for the strength and spatial extent of the signal of each source, which can tell us about the limitations in strengths and sizes of the source signal that the technique is able to correctly invert. Figure 8a shows the absolute value of the angular difference between the true and the estimated dipole moment vectors. Figure 8b shows the percentage difference between the true and estimated dipole moment magnitudes ( $|100 (m_{true} - m_{estimated}) / m_{true}|$ ). Figure 8c shows the  $R^2$  coefficient (Equation 21), which is equivalent to the non-dipolarity parameter of Fu et al. (2020) and represents how well the dipolar model

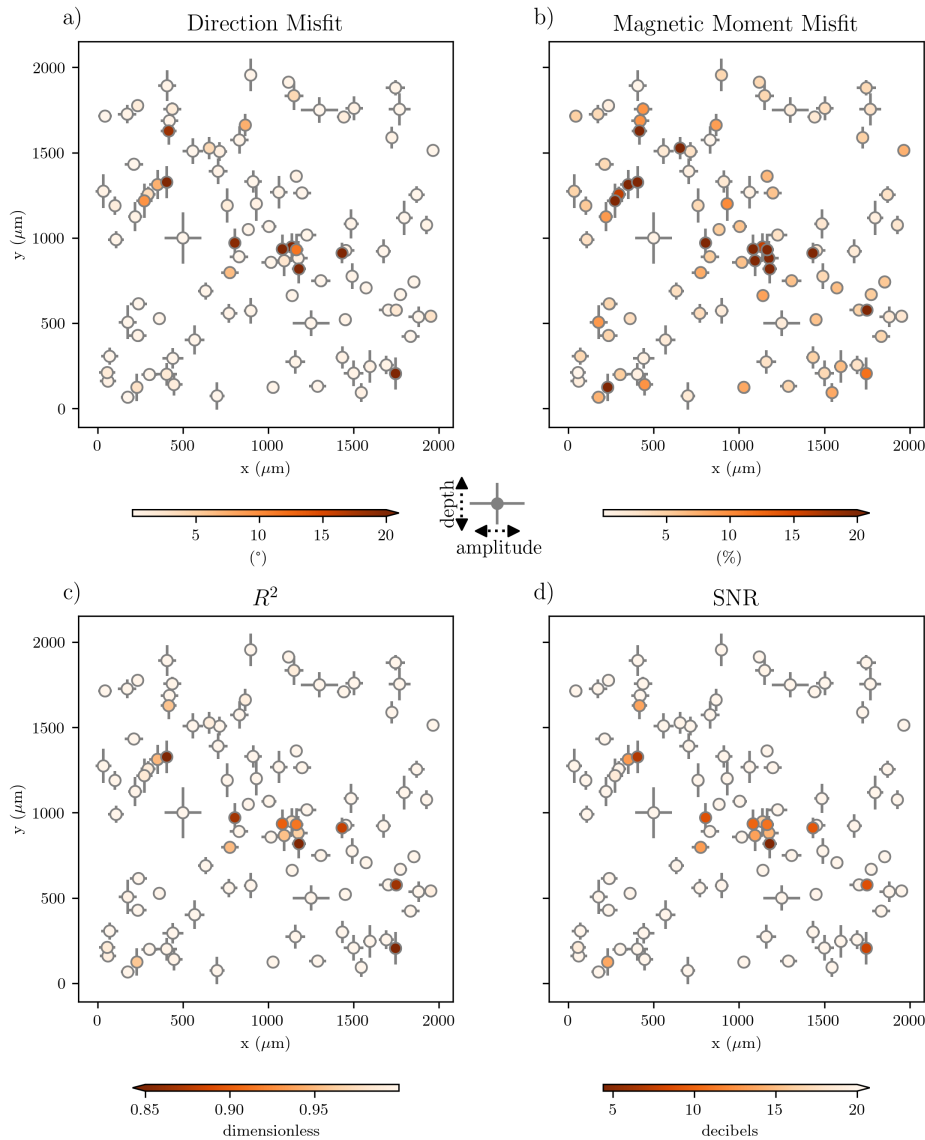


**Figure 8:** The validation of the result obtained with the inversion was calculated for each individual particle based on the error between the real parameters modeled and their respective recovered values, being (a) the direction and (b) intensity of the magnetic moment, in addition to the  $R^2$  score (c) obtained by comparing the forward model and the actual data. The depth and radius of the magnetic sources are also important factors that influence the final result, therefore, these data are given in the form of cross plots, with the vertical bar represented by the depth (1 - 20  $\mu\text{m}$ ) and the horizontal bar by the dipole moment amplitude ( $10^{-12}$  to  $10^{-14} \text{Am}^2$ ).

is able to explain the observed data of each source. Figure 8d shows the SNR (Equation 22), which expresses the power of the observed data over that of the inversion residuals. High SNR values correspond to small inversion residuals which indicate that a dipolar model was able to explain the observed data. Consequently, the variation of SNR values is similar to that of the  $R^2$  coefficient. Figure 8 shows that large errors in the estimated dipole moment direction are associated with low values of  $R^2$  and SNR. Conversely, the correlation between errors in dipole moment magnitude and  $R^2$  and SNR is less pronounced, with some poor magnitude estimates being associated with  $R^2$  and SNR indicating a good fit of the dipolar model. It is also noticeable that the majority of cases where the dipole moment direction error is large are associated with deep and low-amplitude sources that

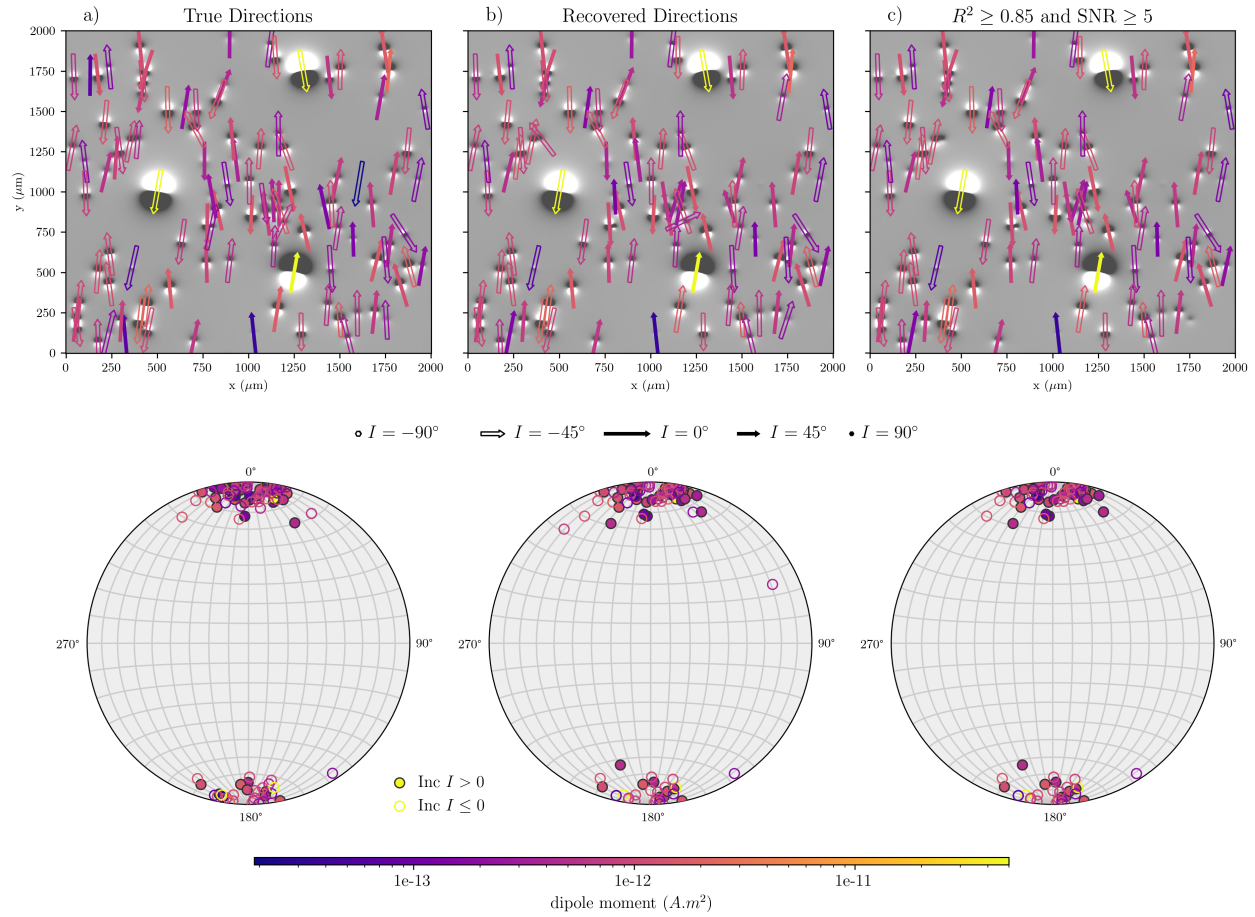


**Figure 9:** Comparison of true and estimated dipole magnetic moments and directions for the complex synthetic sample. a) Simulation of a thin section of rock with 103 particles uniformly magnetized (dipolar sources) by two different induced fields. The average directions of the induced fields are  $D = 0^\circ$  and  $I = 0^\circ$  and  $D = 180^\circ$  and  $I = 0^\circ$ , yielding two stable directions. b) All estimated vector directions of the identified sources ( $M = 99$ ). c) The Filtering criteria used to select the magnetic directions of the sources with the best fitting ( $M = 96$ ), determined by the coefficient of determination ( $R^2 \geq 0.85$ ) and signal-to-noise ratio ( $\text{SNR} \geq 5$ ).

are close to shallower or higher-amplitude sources. These results indicated that  $R^2$  and SNR can be used as selection criteria to discard sources with likely high errors in the estimated dipole moment.

Figure 9 shows stereograms with the directions generated by the modeled (Figure 9a) and the estimated vectors (Figure 9b) for each source. The distribution of the estimated directions is coincident with the true directions aside from a few sources, the same ones with the higher values of direction misfit (Figure 8a) which is probably associated with the mutual interference of sources close to each other or within the same window. When filtered to include only data with  $R^2 > 0.85$  and  $\text{SNR} > 5$  the obtained direction distribution is closer to the true distribution (Figure 9c).

## 4 Application to real data

To test whether the proposed method would be able to determine the magnetization directions and the magnetic moment of particles in natural samples, we selected a previously studied carbonate sta-

lagmite sample from the Wintimdouine cave in the Agadir region (Morocco) (Ait Brahim et al., 2019). This speleothem contains both magnetite and hematite as the main carriers of magnetic remanence, as attested by thermomagnetic curves with temperature decays at  $\sim 580$  °C and  $\sim 680$  °C, and bimodal curves of isothermal remanent magnetization (IRM) acquisition (Carmo et al., 2019).

In order to provide two distinct directions associated with the different magnetic mineral types in this sample, we applied two IRM pulse fields of 2.7 T and 0.3 T, respectively toward the +Y and -Y directions. In this way, the high coercivity grains (hematite) would point towards +Y and the low coercivity ones (magnetite) would align in the -Y direction.

After remanence acquisition, we performed a magnetic map with the Quantum Diamond Microscope (QDM) at Harvard University over a sample section of approximately  $1410 \mu\text{m} \times 2256 \mu\text{m}$  (Figure 10a) with a grid spacing of  $2.35 \mu\text{m}$  and a sensor-sample distance of approximately  $5 \mu\text{m}$ , totaling 576,000 data points. The QDM is housed in a shielded room, in order to avoid the influence of the Earth's magnetic field while the data were taken in projected magnetic microscopy (PMM) mode and converted to the vertical component of magnetic field ( $b_z$ ) using a spectral approach (Fu et al., 2020; Glenn et al., 2017; Lima and Weiss, 2009). We applied a bias field of 0.9 mT during the measurement, which was periodically reversed to result in an effective background field of  $< 1 \mu\text{T}$ . After applying the magnetic anomaly detection algorithm (Figure 10b-e), it was possible to determine the windows for 75 potential sources, as shown in Figure 10e.

After applying the ED algorithm, we performed the inversion of the magnetic moment for each of the 75 windows selected previously. In order to reduce considerably the computation time, the inversions were done within each data window, instead of solving all sources parameters at the same time. We obtained the magnetic moment and the direction for all 75 magnetic grains (Figure 11a). Then, we calculated the residuals of the inversions in each window and subsequently the coefficient of determination  $R^2$  and signal-to-noise ratio (SNR), which were parameters used as filters for the best directions obtained. We considered a good fit to be achieved when  $R^2$  was greater or equal to 0.85 and SNR was greater than 5. An  $R^2$  value of 0.85 indicates that 85 % of the measured magnetic data is explained by the predicted dipole model, which is equivalent to the dipolarity test approach (Fu et al., 2020). On the other hand, an SNR of 5 means that the dipolar signal is 5 times greater than the residual noise. By using these criteria, we ensured that the fit was sufficiently accurate and the dipole model provided a reliable approximation of the original magnetic data. About 46 identified sources passed these criteria. This filtering technique removed the poorly fit predicted models as well as the ones too corrupted with noise, showing more clearly the expected directional clusters of hematite and magnetite crystals (Figure 11b). Notably, it is confirmed that the sample has both magnetic minerals, but by the expected directions we can also stipulate that the magnetite grains outnumber the hematite ones.

## 5 Discussion

### 5.1 Prior information and uniqueness of solutions

Working with potential field data might be very tricky once there is too much ambiguity involved during data modeling, thus to obtain unique and reliable results from data inversion it is necessary to provide as much prior information as possible. One way to circumvent the ambiguity is to incorporate prior information about the subsurface structure, such as the positioning of a known source of magnetization. Magnetic field measurements are more sensitive to changes in magnetization near

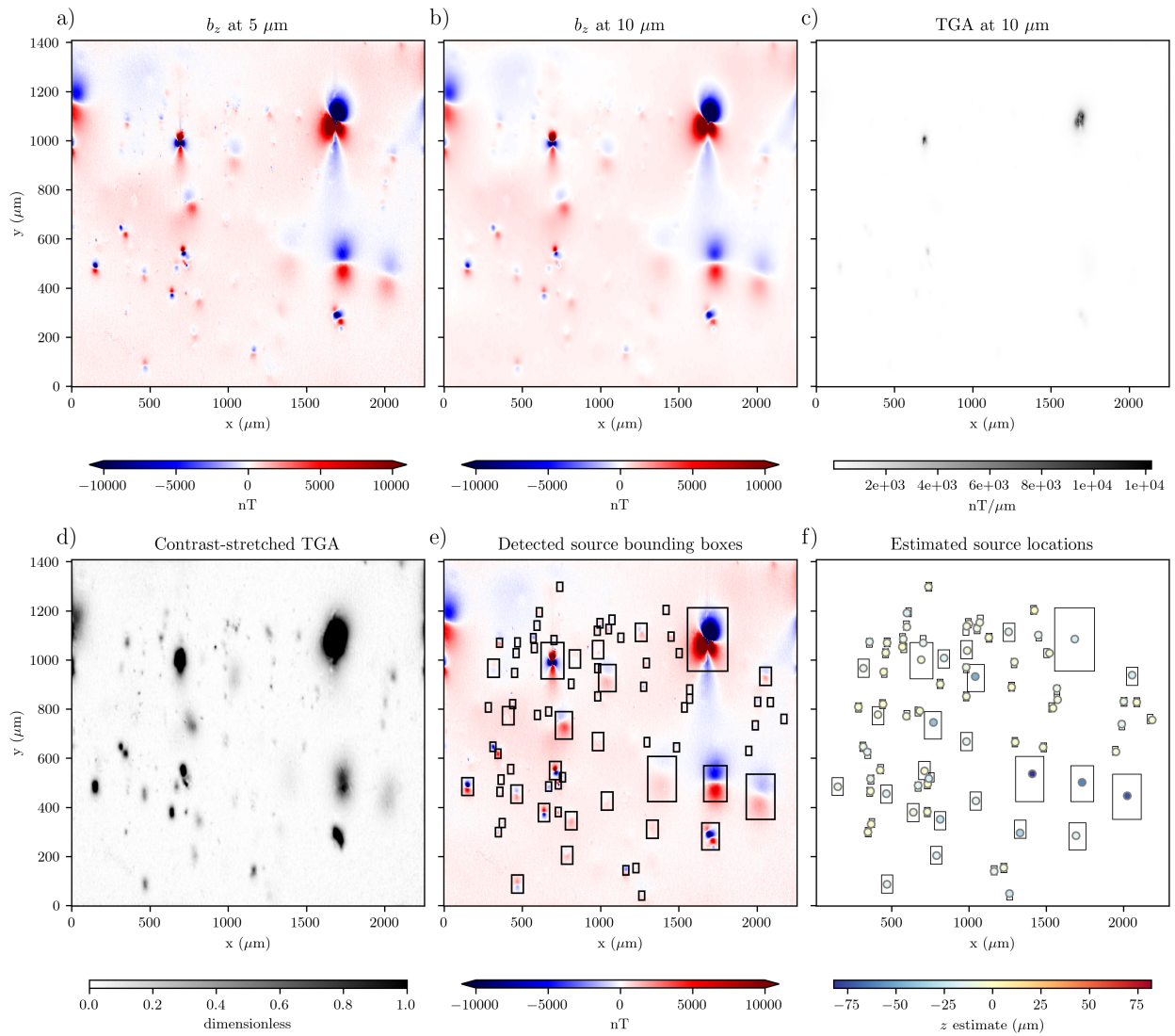


**Figure 10:** Real data and the various processing steps performed prior to the dipole moment inversion. a) The real sample vertical component magnetic data  $b_z$  observations at  $z = 5 \mu\text{m}$ . b) Anomaly map after the upward-continued data to  $z = 10 \mu\text{m}$  to attenuated long and short-wavelength noise. c) The total gradient amplitude (TGA) calculated from the upward-continued data. d) The contrast-stretched TGA. e) The detected source bounding boxes (black squares) that correctly encapsulate the main signal of the sources. f) The estimated source locations (colored circles) from Euler Deconvolution of the upward-continued data inside each bounding box. The color represents the estimated  $z$  coordinates.

the source that is causing the anomaly. When the position of the source is known, it constrains the model to be as consistent as possible with the observed data, hence increasing the likelihood of obtaining unique solutions. Oliveira Jr. et al. (2015) proved that the magnetization directions (Dec and Inc) recovered by the least squares estimator are sensitive to great variations in the horizontal coordinates of the center of the magnetic sources, but are practically insensitive to variations in depth. Thus, they consider the ED method as an adequate technique to estimate the central positions that will be used as prior information for inversion. This occurs mainly because, when well performed, the recovery of the source's horizontal coordinates is considerably accurate, while the vertical coordinate can undergo greater variation even though it still provides satisfactory results (Melo et al., 2013; Silva and Barbosa, 2003). This remark is also better observed in our simple synthetic sample

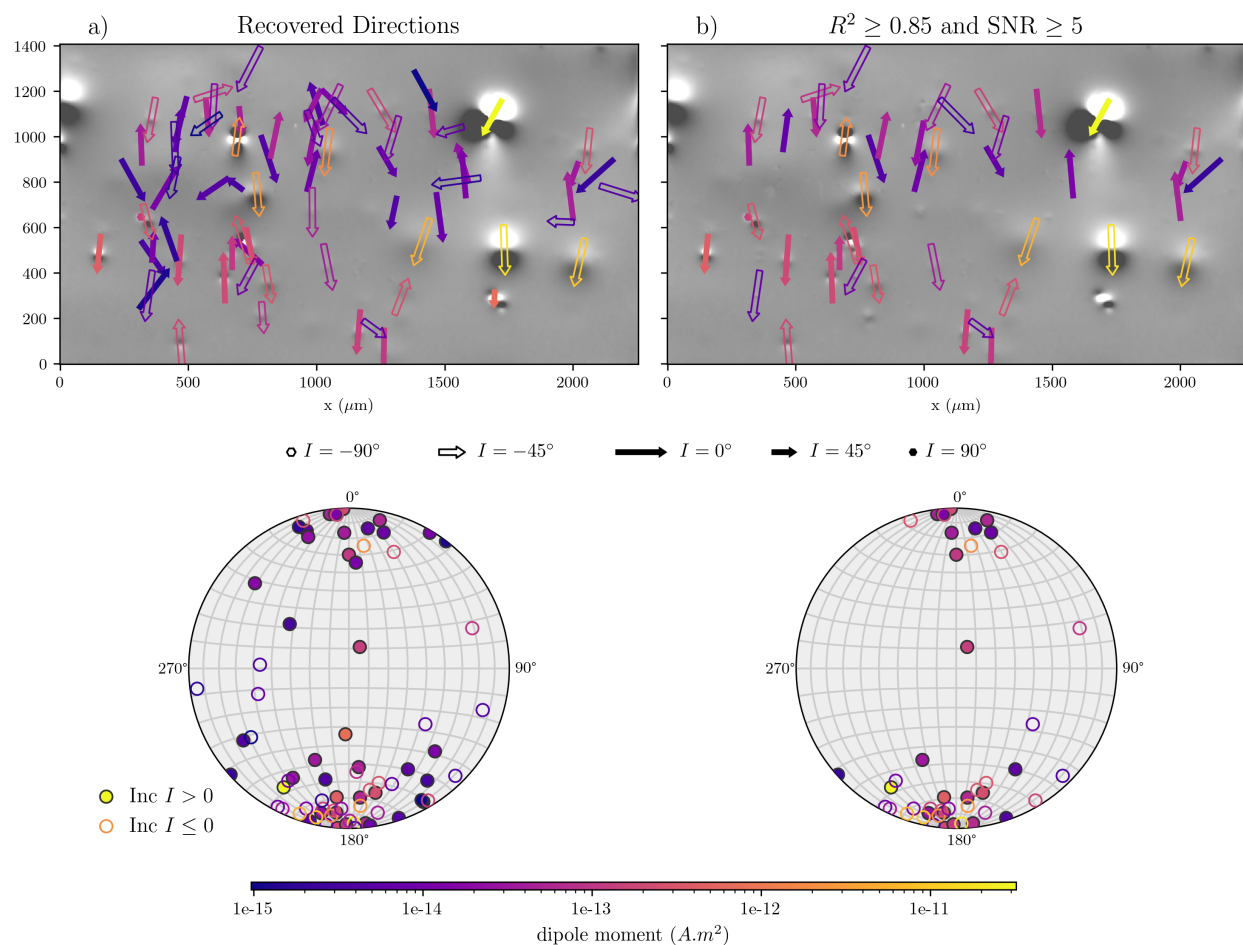


**Figure 11:** Comparison of the estimated dipole magnetic moments and directions for the real data sample. a) All estimated directions without filtering ( $M = 75$ ). b) Estimated directions filtered ( $M = 46$ ) by the coefficient of determination ( $\geq 0.85$ ) and SNR ( $\geq 5$ ), which shows two clusters of direction located on each pole of the stereogram.

where the estimated horizontal positions slightly deviate from the true values, which implies small misfit values in the recovered magnetic directions. Although the estimated magnetic moment for the said sample is satisfactory, this magnetic parameter is more affected by the variations in the depth of the source, which is probably caused by ambiguities. In summary, in order to estimate all magnetic parameters as precisely as possible the ED must be executed within a data window containing the lowest amount possible of noise since that high-frequency noise sensibility is one of the ED's main limitations.

## 5.2 A critical examination of the source detection

Since the pioneering work of Egli and Heller (2000), many methodologies were proposed for solving the inverse problem of micromagnetic data, and for the purpose of comparison we separate them into two categories based on the main estimated parameter by the inversion procedure. In the first type of approach, the main goal is usually to estimate average magnetization by inverting the whole sample superficial magnetization data commonly by means of unidirectional problem, uniform di-

rections with non-negative variable dipole moments (e.g., [Weiss et al., 2007](#)), including performance enhancement in the spatial domain (e.g., [Myre et al., 2019](#)) or frequency domain (e.g., [Lima et al., 2013](#)). This methodology can be used to remarkably estimate the average magnetic direction and the total moment direction with the assumption that the particles were all magnetized in the direction of the same induced field (sIRM and/or NRM in basalts, [Weiss et al., 2007](#)). However, this assumption is not always true when dealing with complex samples (i.e., more than one stable direction), which leads to the same drawbacks as the classic paleomagnetic measurements using bulk samples. The second type of approach has the goal of finding the individual source magnetic properties, which can be done by either inverting the dipole moment of a single source within a cropped section of an upward continued anomaly map (e.g., [Fu et al., 2020](#); [Lima and Weiss, 2016](#)) or by the insertion of additional information of the sources' shape, such as micro-computed tomography (microCT) (e.g., [de Groot et al., 2021, 2018](#); [Fabian and de Groot, 2019](#)). The latter further allows unique estimation of magnetic moment configuration of even higher orders components through spherical harmonics expansion constrained by micromagnetic models (e.g., [Cortés-Ortuño et al., 2021, 2022](#)). Such outstanding techniques come with some troubles of having to mechanically select the data for inversion or dealing with the weaknesses of the additional method used. The MicroCT, for example, is a popular non-destructive technique for high-resolution imaging of the material internal structures, and yet, it is accompanied by some limitations when it comes to paleomagnetic studies: firstly, the technique has a spatial resolution on the order of micrometers, which is not sufficient to directly image the fine grained single-domain magnetite ([de Groot et al., 2018](#)). The microCT also struggles to discern ferromagnetic (*l.s.*) from non-magnetic/antiferromagnetic minerals, as pointed out by [de Groot et al. \(2021\)](#), since they usually have similar densities and therefore similar X-ray attenuation ([Cnudde and Boone, 2013](#)). In any case, the major limitation of microCT lies in the trade-off between the resolution and the sample size, requiring small sample volumes to achieve higher resolutions causing the technique to be too time-consuming.

Our proposed methodology has the goal of finding each individual source's dipole moment components without the trouble of mechanically selecting cropped data or needing any type of additional information. However, to better examine its advantages and disadvantages we first need to point out the strengths and weaknesses of the technique used in the detection of sources, the Laplacian of Gaussian (LoG) kernel ([Marr and Hildreth, 1980](#)). The LoG is a computer imaging technique that is able to identify regions where the intensity changes abruptly by convolving the image with the LoG filter, and is the result of the combination of the Gaussian blur and Laplacian filter ([Gonzalez and Woods, 2018](#)). The Laplacian filter is able to highlight the regions where the intensity changes rapidly. On the other hand, the Gaussian blur is a smoothing filter for high-frequency noise, which reduces the likelihood to generate artifacts. Hence, the result of this LoG operation can identify blobs as regions above a certain threshold, this threshold crossing determines what are brighter spots (local maxima) surrounded by a darker background. It is also scale-invariant by detecting blobs of different sizes and intensities, a feature achieved by varying the sizes of the Gaussian filter. The advantages of the methodology are (i) high-accuracy blob detection; (ii) scale-invariant for images with different intensities/sizes of objects; while also being (iii) robust to the presence of noise due to the Gaussian smoothing filter. While the main drawbacks of the LoG blob algorithms are: (i) being computationally expensive/time-consuming when dealing with larger images and (ii) the requirement of parameter adjustments, such as the threshold and the kernel sizes.

The total gradient anomaly (TGA) might be considered the ideal image to be used as input for the LoG blob detection algorithm for potential field studies (micro and/or macroscale). The TGA

highlights the subsurface sources by generating a map of positive magnetic anomalies concentrated within their edges. This technique is widely used in aeromagnetic surveys to determine the boundaries of sources by calculating the magnetic gradient in all Cartesian directions and displaying those regions where the gradient has maximum values, which is a local maxima distribution. Hence. The application for micromagnetic measurements comes with all the advantages and drawbacks previously mentioned because is highly dependent on the selection of a good data window. Nonetheless, the windows generated isolate the main magnetic signal's region of each source. This guarantees that our thresholding approach (see section 5.3), for both ED and dipolar inversion, is performed using the critical slice of the micromagnetic data, giving satisfactory parameters approximation and fast results as shown in the synthetic data.

The complex synthetic data allows better observation of the strengths and limitations of the windows approach. The main strengths that can be mentioned are: (i) the applied technique not only detects most of the modeled sources but also (ii) most of the recovered magnetic parameters have considerably low errors, especially in the directions, usually less than  $5^\circ$  (Figure 8a). (iii) The magnetic moments obtained from well-individualized sources tend to not deviate much from the real values (Figure 8b) when  $R^2$  and SNR scores are considered high ( $\geq 0.85$  and  $\geq 5$ , respectively) (Figure 8c-d). (iv) Shallow particles grouped in clusters are usually well individualized during window selection, as well as (v) some isolated particles that produce a weak magnetic signal. The major limitations observed were: (i) the blob detection fails when there are sources too close, grouping them into the same window, thus causing an erroneous result both for Euler deconvolution and for the magnetic parameters. (ii) The very same occurs when there is a source under another, in this case, the magnetic signal is the sum of both. (iii) In clusters of larger and/or deeper particles, although the method individualizes them well, the magnetic signal of the neighboring particles can considerably influence the result of the inversion, especially the estimated dipole moment (cluster in the Figure 8b with the highest misfit values). As expected, there is a direct relationship between the dipole intensity and depth with the observed errors. It is clear from the error bars in Figure 8 that deep-seated sources and/or particles with small dipole moments generate worse results, essentially because they will produce weaker anomalous fields in the magnetic maps. Note nonetheless, that even sources with small dipole moments when close to the surface are adequately modeled by our method, because of the trade-off between signal and noise for grains near the sensor.

### 5.3 Reliability of dipole moment approximation

Our approach relies in the premise of assuming the magnetic anomaly within the data window is a response of a dipolar source. The latter is true when working with particle signals in the SD magnetic domain state since they are uniform magnetized particles with strong dipolar anomalies. However, Nagy et al. (2017) reported that particles within the PSD domain can record the paleomagnetic field for longer (than SD ones) periods of time, being the stabler and also with strongly non-dipolar characteristics. Therefore the application of the proposed algorithm to natural samples should fail for those PSD particles. Cortés-Ortuño et al. (2022) give important insights about the matter; they showed that PSD state particles present more accurate inversion results when considering the non-dipole components for small sample-sensor distances ( $<1 \mu\text{m}$ ), but for larger sensor distances the dipole as approximations are remarkably accurate, as the higher-order moments decay rapidly with distance and therefore have less influence on the particle's magnetic signal. Thus, our approach can be considered reasonable to work with both particle SD and PSD states signals. The latter happens mainly due to the sensor height being usually greater than  $5 \mu\text{m}$ , considering a particle on the immediate

surface of the sample the higher-order moments are already quite attenuated, thus circumventing the prominent problems described for non-dipolar components. This is corroborated by our non-dipolar synthetic sample showing the almost complete attenuation of non-dipolar components at distances greater than  $5 \mu\text{m}$ .

Despite the excellent signal-to-noise ratio that the SMM provided with the proximity of the sensor to the sample, it is worth mentioning that the measurement noise can still overshadow the responses of very weak/small, or deep particles, generating unreliable inversion results. Therefore, it is necessary to keep a check to determine if the inversion reached a satisfactory prediction, such as the coefficient of determination and the signal-to-noise ratio suggested by (Cortés-Ortuño et al., 2021).

While the windows approach violates the fundamental theory of the inversion problem that requires the sampled area to be finite and encapsulated by the inversion domain to ensure the uniqueness of results (Baratchart et al., 2013; Lima et al., 2013), our technique is similar to the one reported by Weiss et al. (2007). The last-mentioned involves thresholding the long-distance interaction of each dipole in the SMM data, which excludes the effect of other dipoles by setting their contribution to zero, resulting in a sparse matrix that permits faster calculations. In contrast to this approach, we employ the TGA map to select the windows and isolate the area containing the main signal of the desired dipole, while the area out of the boundaries of the window is less sensitive to variation in magnetic parameters of this particular source, hence we exclude them from the inversion domain. This technique allows us to obtain the 3D positioning and an approximation of the dipole moment components of hundreds of sources within a few seconds, while the inversion is fast the time bottleneck of our methodology is associated with the blob detection process.

## 6 Conclusion

We developed an efficient semi-automated method to determine the direction of magnetization of dipolar sources on a microscale, as well as the estimate of their magnetic moment. Being ideal for a reinterpretation for the application of methods of paleomagnetic studies using thin sections of rock samples. This would be an attempt to improve the quality of results obtained by isolating the responses of more reliable recorders of the Earth's geomagnetic field.

We also present a new, faster, and cleaner way to solve the Euler equation in determining the positioning of magnetic anomaly sources using a pre-selection of magnetic anomaly source windows based on the Laplacian of Gaussian applied to total gradient anomaly maps. In this way, reducing the numerous solutions to just one data window per source. After estimating the structural index ( $n = 3$ ) by approximating the sources generating the magnetic anomaly to spheres/points, the Euler Deconvolution is performed, and the central position of each source is determined. Due to the similarity with aeromagnetic data, this approach can also be extrapolated for macro-scale studies.

To recover magnetic direction and moment we only need to assume that the sources have their central positions known (so we apply Euler deconvolution) and that their magnetization is uniform. This last premise aligns with the theory of magnetically stable particles SD, and by extension the PSD ones at a reasonable sensor-sample height, which is the basis of classical paleomagnetism. Also, there is no need for any kind of prior knowledge other than the observed magnetic anomaly, and the structural index of the sources. Therefore, this method can be quickly replicated in a data set of thin sections of rocks to obtain the distributions of magnetic directions of each source identified in the sample.

The test using a simple synthetic sample shows the great capability of the method by estimating

not only the precise center positions but also retrieving the magnetization directions and intensity even under the considerable effect of high-frequency noise, for both dipolar and non-dipolar sources. While the complex synthetic sample data allows observing the applicability of the method developed in real samples that are more complex with varied magnetization directions and intensity, in addition to also taking into account the high and low-frequency noise and sources with variable dipole moment intensities and depths. The real sample data positively answered the question of the algorithm's ability to deal with thin sections of rocks. But also, showed the acceptable capacity of retrieving different magnetization directions recorded by magnetic minerals with different coercivities and magnetic signal disparities even greater than predicted in the complex synthetic test. We also assessed the quality of the fit between the predicted dipole model and the original magnetic data using two criteria: the coefficient of determination ( $R^2$ ) and the signal-to-noise ratio (SNR).

## 7 Data and code availability

The Python source code used to produce all results and figures presented here is available at <https://github.com/compeolab/micromag-euler-dipole> and <https://doi.org/10.6084/m9.figshare.22672978> under the MIT open-source license. The QDM magnetic microscopy data are available at [https://figshare.com/articles/dataset/QDM\\_magnetic\\_microscopy\\_dataset\\_of\\_a\\_speleothem\\_from\\_Morocco/22965200](https://figshare.com/articles/dataset/QDM_magnetic_microscopy_dataset_of_a_speleothem_from_Morocco/22965200) under the CC-0 license.

The image re-scaling and blob detection through the Laplacian of Gaussian method were performed with the scikit-image library (Van der Walt et al., 2014). We also used matplotlib (Hunter, 2007) and mplstereonet (Kington, 2020) or generating figures and stereograms. Basic calculations were performed using Numpy (Harris et al., 2020) and Scipy (Virtanen et al., 2020). Verde (Uieda, 2018) was used to generate data grids. Upward continuation was performed using Harmonica (Fatiando a Terra Project et al., 2023). The Choclo library (Fatiando a Terra Project et al., 2022) provided kernel functions used in the forward and inverse problems. The Numba just-in-time compilation library (Lam et al., 2015) was used to speed-up calculations. Lastly, the Xarray library (Hoyer and Hamman, 2017) offered a fast and powerful tool for working with multi-dimensional datasets allowing an easy way of data visualization and extraction with advanced indexing techniques.

## 8 Acknowledgements

We are indebted to the developers and maintainers of the open-source software without which this work would not have been possible. This research was supported by grant 162704/2021-6 from the Conselho Nacional de Desenvolvimento Científico e Tecnológico (CNPq), grant 2021/08379-5 from the Fundação de Amparo à Pesquisa do Estado de São Paulo (FAPESP), and grant IES\R3\213141 from the Royal Society. The opinions, hypotheses, and conclusions or recommendations expressed in this material are the responsibility of the authors and do not necessarily reflect the views of FAPESP.

## References

Ait Brahim, Y., Bouchaou, L., Sifeddine, A., Beraaouz, E. H., Wanaim, A., and Cheng, H. (2019). Hydroclimate characteristics of the karst system of Wintimdouine cave (Western High Atlas, Morocco): monitoring and implications for paleoclimate research. *Environmental Earth Sciences*, 78(16). doi:10.1007/s12665-019-8496-5.

- Aster, R. C., Borchers, B., and Thurber, C. H. (2019). *Parameter Estimation and Inverse Problems*. Elsevier, San Diego, USA. ISBN 9780128046517. doi:[10.1016/C2015-0-02458-3](https://doi.org/10.1016/C2015-0-02458-3).
- Baratchart, L., Hardin, D. P., Lima, E. A., Saff, E. B., and Weiss, B. P. (2013). Characterizing kernels of operators related to thin-plate magnetizations via generalizations of Hodge decompositions. *Inverse Problems*, 29(1):015004. doi:[10.1088/0266-5611/29/1/015004](https://doi.org/10.1088/0266-5611/29/1/015004).
- Barbosa, V. C. F. and Silva, J. B. C. (2011). Reconstruction of geologic bodies in depth associated with a sedimentary basin using gravity and magnetic data. *Geophysical Prospecting*, 59(6):1021–1034. doi:[10.1111/j.1365-2478.2011.00997.x](https://doi.org/10.1111/j.1365-2478.2011.00997.x).
- Barnes, C., Majka, J., Schneider, D., Walczak, K., Bukala, M., Kościńska, K., Tokarski, T., and Karlsson, A. (2019). High-spatial resolution dating of monazite and zircon reveals the timing of subduction–exhumation of the Vaimok Lens in the Seve Nappe Complex (Scandinavian Caledonides). *Contributions to Mineralogy and Petrology*, 174(1):5. doi:[10.1007/s00410-018-1539-1](https://doi.org/10.1007/s00410-018-1539-1).
- Berndt, T., Muxworthy, A. R., and Fabian, K. (2016). Does size matter? Statistical limits of paleomagnetic field reconstruction from small rock specimens. *Journal of Geophysical Research: Solid Earth*, 121(1):15–26. doi:[10.1002/2015JB012441](https://doi.org/10.1002/2015JB012441).
- Blakely, R. J. (1996). *Potential Theory in Gravity and Magnetic Applications*. Cambridge University Press, Cambridge.
- Carmo, J. A., Trindade, R. I. F., Jaqueto, P., Cruz, F. W., Brahim, Y. A., and Cheng, H. (2019). Speleothem derived secular variation in morocco for the past 6000 years. In *AGU Fall Meeting Abstracts*, San Francisco. AGU Fall Meeting.
- Cnudde, V. and Boone, M. (2013). High-resolution X-ray computed tomography in geosciences: A review of the current technology and applications. *Earth-Science Reviews*, 123:1–17. doi:[10.1016/j.earscirev.2013.04.003](https://doi.org/10.1016/j.earscirev.2013.04.003).
- Cortés-Ortuño, D., Fabian, K., and de Groot, L. V. (2021). Single Particle Multipole Expansions From Micromagnetic Tomography. *Geochemistry, Geophysics, Geosystems*, 22(4). doi:[10.1029/2021GC009663](https://doi.org/10.1029/2021GC009663).
- Cortés-Ortuño, D., Fabian, K., and Groot, L. V. (2022). Mapping Magnetic Signals of Individual Magnetite Grains to Their Internal Magnetic Configurations Using Micromagnetic Models. *Journal of Geophysical Research: Solid Earth*, 127(5). doi:[10.1029/2022JB024234](https://doi.org/10.1029/2022JB024234).
- Davidson, J. P., Morgan, D. J., Charlier, B. L., Harlou, R., and Hora, J. M. (2007). Microsampling and isotopic analysis of igneous rocks: Implications for the study of magmatic systems. *Annual Review of Earth and Planetary Sciences*, 35:273–311. doi:[10.1146/annurev.earth.35.031306.140211](https://doi.org/10.1146/annurev.earth.35.031306.140211).
- de Groot, L. V., Fabian, K., Bakelaar, I. A., and Dekkers, M. J. (2014). Magnetic force microscopy reveals meta-stable magnetic domain states that prevent reliable absolute palaeointensity experiments. *Nature Communications*, 5(1):1–10. doi:[10.1038/ncomms5548](https://doi.org/10.1038/ncomms5548).
- de Groot, L. V., Fabian, K., Béguin, A., Kosters, M. E., Cortés-Ortuño, D., Fu, R. R., Jansen, C. M., Harrison, R. J., Leeuwen, T., and Barnhoorn, A. (2021). Micromagnetic Tomography for Paleomagnetism and Rock-Magnetism. *Journal of Geophysical Research: Solid Earth*, 126(10):e2021JB022364. doi:[10.1029/2021JB022364](https://doi.org/10.1029/2021JB022364).
- de Groot, L. V., Fabian, K., Béguin, A., Reith, P., Barnhoorn, A., and Hilgenkamp, H. (2018). Determining Individual Particle Magnetizations in Assemblages of Micrograins. *Geophysical Research Letters*, 45(7):2995–3000. doi:[10.1002/2017GL076634](https://doi.org/10.1002/2017GL076634).
- Dunlop, D. J. and Özdemir, O. (1997). *Rock Magnetism Fundamentals and Frontiers*. Cambridge University Press. doi:[10.1017/cbo9780511612794](https://doi.org/10.1017/cbo9780511612794).
- Egli, R. and Heller, F. (2000). High-resolution imaging using a high-Tc superconducting quan-

- tum interference device (SQUID) magnetometer. *Journal of Geophysical Research: Solid Earth*, 105(B11):25709–25727. doi:[10.1029/2000JB900192](https://doi.org/10.1029/2000JB900192).
- Fabian, K. and de Groot, L. V. (2019). A uniqueness theorem for tomography-assisted potential-field inversion. *Geophysical Journal International*, 216(2):760–766. doi:[10.1093/GJI/GGY455](https://doi.org/10.1093/GJI/GGY455).
- Fatiando a Terra Project, Esteban, F. D., Li, L., Oliveira Jr, V. C., Pesce, A., Shea, N., Soler, S. R., Tankersley, M., and Uieda, L. (2023). Harmonica v0.6.0: Forward modeling, inversion, and processing gravity and magnetic data. *Zenodo*. doi:[10.5281/zenodo.7690145](https://doi.org/10.5281/zenodo.7690145).
- Fatiando a Terra Project, Soler, S. R., and Uieda, L. (2022). Choclo v0.0.1: Kernel functions for your geophysical models. *Zenodo*. doi:[10.5281/zenodo.7851748](https://doi.org/10.5281/zenodo.7851748).
- Fu, R. R., Lima, E. A., Volk, M. W., and Trubko, R. (2020). High-Sensitivity Moment Magnetometry With the Quantum Diamond Microscope. *Geochemistry, Geophysics, Geosystems*, 21(8):e2020GC009147. doi:[10.1029/2020GC009147](https://doi.org/10.1029/2020GC009147).
- Glenn, D. R., Fu, R. R., Kehayias, P., Le Sage, D., Lima, E. A., Weiss, B. P., and Walsworth, R. L. (2017). Micrometer-scale magnetic imaging of geological samples using a quantum diamond microscope. *Geochemistry, Geophysics, Geosystems*, 18(8):3254–3267. doi:[10.1002/2017GC006946](https://doi.org/10.1002/2017GC006946).
- Gonzalez, R. C. and Woods, R. E. (2018). *Digital Image Processing*. Pearson, 4th edition. ISBN 9780133356724.
- Han, K. T. M. and Uyyanonvara, B. (2016). A Survey of Blob Detection Algorithms for Biomedical Images. In *7th International Conference of Information and Communication Technology for Embedded Systems (IC-ICTES)*, pages 57–60. IEEE. doi:[10.1109/ICTEmSys.2016.7467122](https://doi.org/10.1109/ICTEmSys.2016.7467122).
- Harris, C. R., Millman, K. J., van der Walt, S. J., Gommers, R., Virtanen, P., Cournapeau, D., Wieser, E., Taylor, J., Bergstra, J., Smith, N. J., Kern, R., Picus, M., Hoyer, S., van Kerkwijk, M. H., Brett, M., Haldane, A., Del Río, J., Wiebe, M., Peterson, P., Gérard-Marchant, P., Sheppard, K., Reddy, T., Weckesser, W., Abbasi, H., Gohlke, C., and Oliphant, T. E. (2020). Array programming with NumPy. *Nature*, 585(7825):357–362. doi:[10.1038/s41586-020-2649-2](https://doi.org/10.1038/s41586-020-2649-2).
- Hoyer, S. and Hamman, J. (2017). xarray: N-D labeled arrays and datasets in Python. *Journal of Open Research Software*, 5(1). doi:[10.5334/jors.148](https://doi.org/10.5334/jors.148).
- Hunter, J. D. (2007). Matplotlib: A 2d graphics environment. *Computing in Science & Engineering*, 9(3):90–95. doi:[10.1109/MCSE.2007.55](https://doi.org/10.1109/MCSE.2007.55).
- Kington, J. (2020). mplstereonet v0.6. URL <https://github.com/joferkington/mplstereonet>. Accessed: 2023-04-21.
- Kong, H., Akakin, H. C., and Sarma, S. E. (2013). A Generalized Laplacian of Gaussian Filter for Blob Detection and Its Applications. *IEEE Transactions on Cybernetics*, 43(6):1719–1733. doi:[10.1109/TSMCB.2012.2228639](https://doi.org/10.1109/TSMCB.2012.2228639).
- Lam, S. K., Pitrou, A., and Seibert, S. (2015). Numba: A llvm-based python jit compiler. In *Proceedings of the Second Workshop on the LLVM Compiler Infrastructure in HPC*, pages 1–6.
- Lima, E. A., Bruno, A. C., Carvalho, H. R., and Weiss, B. P. (2014). Scanning magnetic tunnel junction microscope for high-resolution imaging of remanent magnetization fields. *Measurement Science and Technology*, 25(10):105401. doi:[10.1088/0957-0233/25/10/105401](https://doi.org/10.1088/0957-0233/25/10/105401).
- Lima, E. A. and Weiss, B. P. (2009). Obtaining vector magnetic field maps from single-component measurements of geological samples. *Journal of Geophysical Research: Solid Earth*, 114(6):6102. doi:[10.1029/2008JB006006](https://doi.org/10.1029/2008JB006006).
- Lima, E. A. and Weiss, B. P. (2016). Ultra-high sensitivity moment magnetometry of geological samples using magnetic microscopy. *Geochemistry, Geophysics, Geosystems*, 17(9):3754–3774. doi:[10.1002/2016GC006487](https://doi.org/10.1002/2016GC006487).

- Lima, E. A., Weiss, B. P., Baratchart, L., Hardin, D. P., and Saff, E. B. (2013). Fast inversion of magnetic field maps of unidirectional planar geological magnetization. *Journal of Geophysical Research: Solid Earth*, 118(6):2723–2752. doi:[10.1002/jgrb.50229](https://doi.org/10.1002/jgrb.50229).
- Maldanis, L., Hickman-Lewis, K., Verezhak, M., Gueriau, P., Guizar-Sicairos, M., Jaqueto, P., Trindade, R. I. F., Rossi, A. L., Berenguer, F., Westall, F., Bertrand, L., and Galante, D. (2020). Nanoscale 3d quantitative imaging of 1.88 Ga Gunflint microfossils reveals novel insights into taphonomic and biogenic characters. *Scientific Reports 2020 10:1*, 10(1):1–9. doi:[10.1038/s41598-020-65176-w](https://doi.org/10.1038/s41598-020-65176-w).
- Marr, D. and Hildreth, E. (1980). Theory of edge detection. *Proceedings of the Royal Society of London. Series B. Biological Sciences*, 207(1167):187–217. doi:[10.1098/rspb.1980.0020](https://doi.org/10.1098/rspb.1980.0020).
- Melo, F. F., Barbosa, V. C. F., Uieda, L., Oliveira, V. C., and Silva, J. B. C. (2013). Estimating the nature and the horizontal and vertical positions of 3d magnetic sources using Euler deconvolution. *Geophysics*, 78(6):J87–J98. doi:[10.1190/GEO2012-0515.1](https://doi.org/10.1190/GEO2012-0515.1).
- Myre, J. M., Lascu, I., Lima, E. A., Feinberg, J. M., Saar, M. O., and Weiss, B. P. (2019). Using TNT-NN to unlock the fast full spatial inversion of large magnetic microscopy data sets. *Earth, Planets and Space*, 71(1):14. doi:[10.1186/s40623-019-0988-8](https://doi.org/10.1186/s40623-019-0988-8).
- Nabighian, M. N., Grauch, V. J. S., Hansen, R. O., LaFehr, T. R., Li, Y., Peirce, J. W., Phillips, J. D., and Ruder, M. E. (2005). The historical development of the magnetic method in exploration. *GEOPHYSICS*, 70(6):33ND–61ND. doi:[10.1190/1.2133784](https://doi.org/10.1190/1.2133784).
- Nagy, L., Williams, W., Muxworthy, A. R., Fabian, K., Almeida, T. P., Conbhúí, P. Ó., and Shcherbakov, V. P. (2017). Stability of equidimensional pseudo–single-domain magnetite over billion-year timescales. *Proceedings of the National Academy of Sciences*, 114(39):10356–10360. doi:[10.1073/PNAS.1708344114](https://doi.org/10.1073/PNAS.1708344114).
- Oliveira Jr., V. C., Sales, D. P., Barbosa, V. C. F., and Uieda, L. (2015). Estimation of the total magnetization direction of approximately spherical bodies. *Nonlinear Processes in Geophysics*, 22(2):215–232. doi:[10.5194/npg-22-215-2015](https://doi.org/10.5194/npg-22-215-2015).
- Reid, A. B., Allsop, J. M., Granser, H., Millett, A. J., and Somerton, I. W. (1990). Magnetic interpretation in three dimensions using Euler deconvolution. *GEOPHYSICS*, 55(1):80–91. doi:[10.1190/1.1442774](https://doi.org/10.1190/1.1442774).
- Roest, W. R., Verhoef, J., and Pilkington, M. (1992). Magnetic interpretation using the 3-D analytic signal. *GEOPHYSICS*, 57(1):116–125. doi:[10.1190/1.1443174](https://doi.org/10.1190/1.1443174).
- Saleh, S. and Pašteka, R. (2012). Applying the regularized derivatives approach in Euler deconvolution and modeling geophysical data to estimate the deep active structures for the northern Red Sea Rift region, Egypt. *Contributions to Geophysics and Geodesy*, 42(1). doi:[10.2478/v10126-012-0003-x](https://doi.org/10.2478/v10126-012-0003-x).
- Silva, J. B. C. and Barbosa, V. C. F. (2003). 3d Euler deconvolution: Theoretical basis for automatically selecting good solutions. *GEOPHYSICS*, 68(6):1962–1968. doi:[10.1190/1.1635050](https://doi.org/10.1190/1.1635050).
- Strum, A. and Fenigstein, A. (2014). Complementary metal-oxide-semiconductor (CMOS) X-ray sensors. In *High Performance Silicon Imaging*, pages 348–372. Elsevier. doi:[10.1533/9780857097521.2.348](https://doi.org/10.1533/9780857097521.2.348).
- Tauxe, L., Banerjee, S. K., Butler, R. F., and Van der Voo, R. (2018). *Essentials of Paleomagnetism: Fifth Web Edition*. [Online; accessed 2021-04-15].
- Thompson, D. T. (1982). Euldp: a new technique for making computer-assisted depth estimates from magnetic data. *Geophysics*, 47(1):31–37. doi:[10.1190/1.1441278](https://doi.org/10.1190/1.1441278).
- Uieda, L. (2018). Verde: Processing and gridding spatial data using Green’s functions. *Journal of Open Source Software*, 3(29):957. doi:[10.21105/joss.00957](https://doi.org/10.21105/joss.00957).
- Van der Walt, S., Schönberger, J. L., Nunez-Iglesias, J., Boulogne, F., Warner, J. D., Yager, N., Gouillart, E., and Yu, T. (2014). scikit-image: image processing in Python. *PeerJ*, 2:e453. doi:[10.7717/peerj.453](https://doi.org/10.7717/peerj.453).

- Verberne, R., Reddy, S. M., Saxey, D. W., Fougereuse, D., Rickard, W. D. A., Plavsa, D., Agangi, A., and Kylander-Clark, A. R. C. (2020). The geochemical and geochronological implications of nanoscale trace-element clusters in rutile. *Geology*, 48(11):1126–1130. doi:[10.1130/G48017.1](https://doi.org/10.1130/G48017.1).
- Virtanen, P., Gommers, R., Oliphant, T. E., Haberland, M., Reddy, T., Cournapeau, D., Burovski, E., Peterson, P., Weckesser, W., Bright, J., van der Walt, S. J., Brett, M., Wilson, J., Millman, K. J., Mayorov, N., Nelson, A. R. J., Jones, E., Kern, R., Larson, E., Carey, C. J., Polat, I., Feng, Y., Moore, E. W., Vand erPlas, J., Laxalde, D., Perktold, J., Cimrman, R., Henriksen, I., Quintero, E. A., Harris, C. R., Archibald, A. M., Ribeiro, A. H., Pedregosa, F., van Mulbregt, P., and Contributors (2020). SciPy 1.0: Fundamental Algorithms for Scientific Computing in Python. *Nature Methods*, 17(3):261–272. doi:[10.1038/s41592-019-0686-2](https://doi.org/10.1038/s41592-019-0686-2).
- Weiss, B. P., Lima, E. A., Fong, L. E., and Baudenbacher, F. J. (2007). Paleomagnetic analysis using SQUID microscopy. *Journal of Geophysical Research: Solid Earth*, 112(9):9105. doi:[10.1029/2007JB004940](https://doi.org/10.1029/2007JB004940).